

STRUCTURE-PROPERTY RELATIONSHIPS OF SOLID STATE ADDITIVE
MANUFACTURED ALUMINUM ALLOY 2219 AND INCONEL 625

by

OSCAR G. RIVERA ALMEYDA

PAUL G. ALLISON, COMMITTEE CHAIR
J. BRIAN JORDON
LUKE N. BREWER
MARK E. BARKEY
CHARLES A. MONROE

A DISSERTATION

Submitted in partial fulfillment of the requirements for
the degree of Doctor of Philosophy
in the Materials Science Program
in the Graduate School of
The University of Alabama

TUSCALOOSA, ALABAMA

2017

Copyright Oscar G. Rivera Almeyda 2017
ALL RIGHTS RESERVED

ABSTRACT

In this investigation, the processing-structure-property relations are correlated for solid state additively manufactured (SSAM) Inconel 625 (IN625) and a SSAM aluminum alloy 2219 (AA2219). This is the first research of these materials processed by a new SSAM method called additive friction stir (AFS). In the case of the AFS IN625, Electron Backscatter Diffraction (EBSD) observed dynamic recrystallization and grain refinement during the layer deposition in the AFS specimens, where the results identified fine equiaxed grain structures (1 micron) formed by dynamic recrystallization (DRX) with even finer grain structures (0.27 microns) forming at the layer interfaces. Additionally, this is the first study to report on the strain rate dependence of AFS IN625 through quasi-static (QS) (0.001/s) and high strain rate (HR) (1500/s) tensile experiments using a servo hydraulic frame and a direct tension-Kolsky bar, respectively, which captured both yield and ultimate tensile strengths increasing as strain rate increased. Fractography performed on specimens showed a ductile fracture surface on both QS, and HR. Alternatively, for the other AFS material system investigated in this study, AA2219, EBSD was performed in the cross-section of the AA2219, also exhibiting DRX with equiaxed microstructure in the three directions and an average grain size of 2.5 microns and the EBSD PFs showed that the material has a torsional fiber A texture. TEM showed that there are no θ' precipitates in the as-deposited cross-section, therefore no precipitation strengthening should be expected. Strain rate and stress state dependence was study, and in both tension and compression, with an increase in strain rate, the YS increase and the UTS decreased. Ductile

fracture surface was observed on specimens tested to failure in both QS and HR. An internal state variable (ISV) plasticity-damage model was used to capture the different yield stress, work hardening and failure strain in the AFS AA2219 for high fidelity modeling of AFS components. The ISV plasticity model successfully captured the material behavior in tension, compression, tension-followed-by-compression and compression-followed-by-tension experiments. Furthermore, the damage parameters of the model were calibrated using the final void density measured from the fracture surfaces.

DEDICATION

I would like to dedicate this dissertation work to my family and friends for all the support through this journey. Especially my parents that have been encouraging me since day one.

ACKNOWLEDGMENTS

I would like to thank my advisor and friend Dr. Paul Allison, for all his support, help and guidance throughout the course of this work. I'm also grateful for Dr. Allison's family, for treating me like part of theirs.

I'm thankful for the valuable insight and assistance provided by my committee members: Dr. J. Brian Jordon, Dr. Luke N. Brewer, Dr. Mark E. Barkey, and Dr. Charles A. Monroe.

Thanks to Rich Martens, Tian Liu, Johnny Goodwin, and Robert Holler for all their assistance with instrument operation in the Central Analytical Facility (CAF), and to my fellow colleagues, for their valuable discussions and experimental assistance that helped shape this project in many ways.

I also want to acknowledge the generosity of Nanci Hardwick and Aeroprobe Corporation for donating the material that made this research possible. Finally, I would like to thank my family and friends, for without their love and encouragement, this dissertation would not have been possible without them.

CONTENTS

ABSTRACT	ii
DEDICATION	iv
ACKNOWLEDGMENTS	v
LIST OF TABLES	viii
LIST OF FIGURES	ix
CHAPTER 1 INTRODUCTION	1
1.1. Research Justification	1
1.2. Materials	2
<i>1.2.1. Microstructure of Inconel 625</i>	2
<i>1.2.2. Mechanical Properties of Inconel 625</i>	3
<i>1.2.3. Microstructure of Aluminum Alloy 2219</i>	4
<i>1.2.4. Mechanical Properties of Aluminum Alloy 2219</i>	6
1.3. Objectives	7
1.3.1. Specific Objectives	8
1.4. Chapter Preface	8
CHAPTER 2 MICROSTRUCTURES AND MECHANICAL BEHAVIOR OF INCONEL 625 FABRICATED BY SOLID-STATE ADDITIVE MANUFACTURING	10
2.1. Introduction	10
2.2. Materials and Methods	13
2.3. Results and Discussion	15

2.4. Conclusions	26
CHAPTER 3 INFLUENCE OF STRESS-STATE AND STRAIN RATE DEPENDENCE OF SOLID STATE ADDITIVE MANUFACTURED AA2219	28
3.1. Introduction	28
3.2. Materials and Methods	31
3.3. Results and Discussion	36
3.4. Conclusions	49
CHAPTER 4 PLASTICITY AND DAMAGE MODELING OF THE BAUSCHINGER EFFECT IN ADDITIVE MANUFACTURED AFS-DEPOSITION AA2219	51
4.1. Introduction	51
4.2. Model Set-up and Calibration on AFS-Deposition AA2219	54
4.2.1. Additive Manufactured AFS-Deposition Material	54
4.2.2. Experimental Procedure	55
4.3. Results and Discussion	57
4.4. Conclusions	65
CHAPTER 5 CONCLUSIONS AND FUTURE WORK	67
5.1. Conclusions	67
5.2. Recommendations and Future Work	69
REFERENCES	71
APPENDIX	79

LIST OF TABLES

Table 2-1. Chemical composition of IN625.	13
Table 2-2. Comparison of IN625 microstructure, YS and UTS of different manufacturing processes.	23
Table 3-1. Chemical composition of AA2219 [61].	32
Table 3-2. Comparison of AA2219 YS, UTS, and ϵ_f of different manufacturing processes.	49
Table 4-1. Chemical composition of AA2219 [61].	55
Table 4-2. Average values of particle size diameter, particle area fraction, particle nearest neighbor distance and grain size. Data was obtained from the middle of the build in the three directions and averaged.	59
Table 4-3. Bauschinger effect results for different prestrains and directions for AFS AA2219.	62

LIST OF FIGURES

Figure 1-1. AFS-Deposition process starting with powder particles (solid material was used for this research) extruded through a hollow pin tool.	2
Figure 2-1. (A) SSAM process starting with solid filler material extruded through a hollow tool. (B) Schematic of the AFS deposition of IN625 and orientation of the tensile specimens.	13
Figure 2-2. Tensile specimen geometry used for both quasi-static (0.001/s) and high rate (1500/s).	15
Figure 2-3. Optical micrograph comparing the microstructure between (A) as-received IN625 filler material and (B) as-build AFS IN625.	16
Figure 2-4. (A) Euler EBSD maps representative location on sample, (B) Euler EBSD maps of 5 locations along build direction, all images are at the same magnification and same location in the corresponding axis, (C) Average grain size and number of grains (location correlates with the EBSD map locations in A and B).	19
Figure 2-5. (A, D, G) Euler EBSD map representative of the middle location. (B, E, H) Boundary rotation map showing the dominant high angle boundary. (C, F, I) Grain reference orientation deviation map.....	20
Figure 2-6. Tensile results comparing the quasi-static (0.001/s) to the high rate (1500/s). The quasi-static achieved a YS of 730 MPa, UTS of 1072 MPa and strain to failure of 0.32. The high rate high rate achieved a YS of 1587 MPa, UTS of 1592 MPa and a strain to failure of 0.34.	22
Figure 2-7. Fractography of the QS (strain rate of 0.001/s) tensile specimen tested to failure. Image A is an optical micrograph of the fracture surface of QS specimen (500 micron scale bars) aligned with the maximum shear strain plane. Images 2-7B, 2-7C and 2-7D (scale bars are 100, 10 and 1 micron, respectively) are SEM images with increasing magnification with arrows pointing to microvoids in 2-7D.	24

Figure 2-8. Fractography of the HR (strain rate of 1500/s) tensile specimen tested to failure. A is an optical micrograph of the fracture surface of HR specimen (500 micron scale bars) aligned with the maximum shear strain plane. Images 2-8B, 2-8C and 2-8D (scale bars are 100, 10 and 1 micron, respectively) are SEM images at increasing magnifications with arrows pointing to the microvoids in 2-8D.25

Figure 2-9. (A) SEM image of tensile specimen with crack parallel to loading direction (other side of Figure 2-6A). (B) SEM image of area analyzed with EBSD. (C) Euler EBSD map representative of the middle location. (D) Boundary rotation map showing the dominant high angle boundary. (E) Grain reference orientation deviation map. (F) Close-up of the crack region in the grain reference orientation deviation map.26

Figure 3-1. (A) SSAM process with solid filler material extruded through a hollow tool. (B) Schematic of the AFS deposition of AA2219 identifying the longitudinal, transverse and build directions.32

Figure 3-2. Locations of the vickers microhardness testing along the as-build AFS2219. ...34

Figure 3-3. Schematic of the microindentation grid used to analyze the transverse cross-section in the three different locations.35

Figure 3-4. Inverse pole figure (IPF) orientation map comparing the microstructure between (A) as-received AA2219-T851 filler material and (B) as-build AFS AA2219. Note the difference in scales between the two maps.37

Figure 3-5. 3D IPF orientation map microstructure representation of the (A) as-received AA2219-T851 filler material (100 μm scale bars), compared to the (B) as-build AFS-Deposited AA2219 material (15 μm scale bars). Arrows point to the direction that the material is feed through the tool of the AFS process.38

Figure 3-6. Hardness bar chart of the AFS-Deposited AA2219 on the transverse cross-section of the deposited material, with error bars representing minimum and maximum values recorded in that layer. EBSD IPF maps of the top, middle and bottom of the deposition with the corresponding grain size are shown. In the y-axis, 0 is the top and 6 is the bottom of the deposition. There are a total of 6 layers with an average thickness of 1 mm. A load of 0.1kgf held for 10s was used for the hardness tests, as described in ASTM E384-16.39

Figure 3-7. EBSD Texture plots of the AFS-Deposited AA2219 build direction (A) representing the texture in the top of the build, (B) the middle, and (C) the bottom.40

Figure 3-8. Re-drawn image representing one of the four ideal torsional orientations for FCC aluminum as reported by F. Montheillet et al. [67].41

Figure 3-9. EBSD Texture plots of the AFS-Deposited AA2219 build direction (observing from the top) (A) representing the texture in the top of the build, (B) the middle, and (C) the bottom.41

Figure 3-10. TEM micrographs (A) as-received material showing θ' precipitates, (B) bottom, (C) middle, and (D) top, TEM micrographs showing θ precipitates and grain structure from the build cross-section Zone 2 for the AFS-Deposited AA2219 (see Figure 3-6 for reference of locations). (Note: magnification in Figure 3-10 (A) is much higher than B-D).43

Figure 3-11. Compression testing results comparing the long transverse, short transverse, and longitudinal directions in quasi-static (0.001/s) and high rate (2500/s). The quasi-static long transverse, short transverse and longitudinal achieved a YS of 145, 140, and 150 MPa, respectively. The high rate long transverse, short transverse, and longitudinal achieved aYS of 295, 238, and 225 MPa, respectively. All compression tests were stopped at a strain of 0.25.44

Figure 3-12. Tensile results comparing the long transverse and longitudinal directions in quasi-static (0.001/s) and high rate (2500/s). The quasi-static long transverse and longitudinal achieved a YS of 148 and 143 MPa, UTS of 363 and 355 MPa and ϵ_f of 0.24 and 0.26, respectively. The high rate long transverse and longitudinal achieved a YS of 235 and 240 MPa, UTS of 240 and 240 MPa and ϵ_f of 0.37 and 0.37, respectively.46

Figure 3-13. Fractography of QS (strain rate of 0.001/s) tensile specimens tested to failure. 3-10A, 3-10B, 3-10C and 3-10D (scale bars are 200, 100, 10, and 5 micron, respectively) are SEM images.47

Figure 3-14. Fractography of HR (strain rate of 2500/s) tensile specimens tested to failure. 3-11A, 3-11B, 3-11C and 3-11D (scale bars are 500, 100, 10, and 5 micron, respectively) are SEM images.48

Figure 4-1. (A) AFS process with the extrusion of the solid material through the hollow rotating tool layer by layer. (B) Schematic of the AFS deposition of AA2219 identifying the three directions (LD, BD, and TD).55

Figure 4-2. Schematic of specimen orientation in the build material.57

Figure 4-3. EBSD IPF maps showing the grain microstructure in the L, TT, and LT directions.58

Figure 4-4. SEM backscattered images of the θ phase in the LD, TD, and BD directions. ..59

Figure 4-5. Internal state variable plasticity damage model calibration for compression (black) and tension (blue) in QS (0.001/s).60

Figure 4-6. A comparison of the internal state variable plasticity-damage model and experimental data illustrating the Bauschinger effect for AFS AA2219 under different directions (tension followed by compression and vice versa) and different prestrain levels (1% and 3%).	62
Figure 4-7. Experimental values of the ratio of kinematic to isotropic hardening (RKI) plotted against the maximum forward prestrain.	63
Figure 4-8. SEM images of the fracture specimen for the QS (strain rate of 0.001/s). (A) At a magnification of 150x. (B) At a magnification of 8000x.	64
Figure 4-9. Comparison of the number density of voids on the fracture surface (average of experimental data) against the model prediction.	65

CHAPTER 1 INTRODUCTION

1.1. Research Justification

The concept of AFS is built upon the inherent benefits of friction stir welding/processing (FSW/P) in that a robust metallurgical bond is created during solid state processing [18,19]. The AFS-Deposition process feeds metal powder or solid rod through a non-consumable rotating cylindrical tool generating heat and plastically deforming the feedstock material through controlled pressure from the tool as successive layers are built upon a substrate (see Figure 1-1). As each layer is added, the tool height increases to accommodate the subsequent material deposition, forcing the material into the previous layer, thus creating a strong metallurgical bond between the layers. During this process, grain refinement, homogenization, and reduction of porosity is established similarly to traditional friction stir processing by tool force and rotation combined with transverse tool movement. Since this is a solid-state process, AFS-Deposition eliminates common problems such as porosity, hot cracking, elemental segregation and dilution associated with fusion-based techniques. Other impacts on material properties of the build layers such as grain refinement are a benefit of the process. Since deposited materials remain below their melting point, distortion in manufactured parts and substrates are lower when compared to other fusion-based processes. The process temperature is expected to be similar to the peak temperature that exists in the nugget zone of friction stir welding/processing, which is $0.6 - 0.9 T_m$, where T_m is the melting point of the material [18]. AFS-Deposition is highly scalable with

high deposition rates, allowing for AFS-Deposition to coat and repair large parts or build fully-dense additive components.

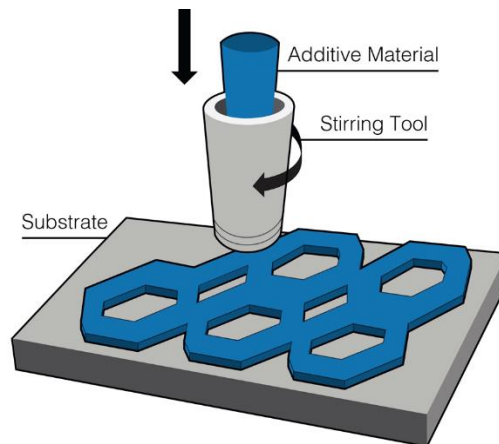


Figure 1-1. AFS-Deposition process starting with powder particles (solid material was used for this research) extruded through a hollow pin tool.

1.2. Materials

1.2.1. Microstructure of Inconel 625

Aeronautic, aerospace, marine and chemical are just a few of the many industries interested in additively manufactured metals with specific properties tailored for highly specialized operating conditions [1–4]. One specific property needed in many of these industrial applications is high temperature mechanical stability, including strength and ductility that is found in superalloys [5–7]. One of these superalloys that has gained wide industrial usage is IN625, a nickel-based superalloy [1]; This alloy has been found to provide a combination of high strength and ductility at temperatures above 1000 °C, as well as the added benefit of oxidation resistance in aggressive environments [8]. The thermo-mechanical SSAM process, AFS-Deposition, provides a new method for additive manufacturing fully-dense IN625 components

with exceptional mechanical properties allowing for unique benefits also applicable for coating, joining, repairing and net shaping applications.

FSW has gained popularity in different industries due to the higher effective weld mechanical properties that may be obtained when compared to fusion welds. This increase in FSW research aided in elucidating some of the microstructural evolution and mechanical behavior phenomenon that may occur during AFS-Deposition processed Inconel alloys [19–21]. Specifically, research by Song and Nakata on FSW IN625 found that the process of FSW recrystallized the grains, thereby improving both the hardness and strength [17]. Similar research on FSW of Inconel 600 also showed benefits of grain refinement to improve the mechanical properties of the weld [22]. However, both investigations observed a decrease in the elongation-to-failure compared to the base material as grain size was refined. Song and Nakata identified grain diameters in the IN625 base material to be between 5 to 15 μm , with an average size of 10.3 μm , whereas in the stir zone the grain diameter was reduced to between 1.3 to 3 μm , with an average size of 2.1 μm [17] exhibiting an equiaxed grain morphology.

1.2.2. Mechanical Properties of Inconel 625

Alternative methods for producing IN625 through additive manufacturing have also been reported in the open literature. Some of these alternative methods include pulsed plasma arc deposition (PPAD) [4], laser aided direct metal deposition (DMD) [8], and laser rapid manufacturing (LRM) [9,10]. These 3D printing techniques [4,8–14] produce columnar dendritic microstructure dependent on the build direction. Additionally, in these additive processes, the reported values of yield strength (YS) and ultimate tensile strength (UTS) were superior to as-cast IN625 [15], but with similar properties to wrought IN625 [16]. Regarding solid state

welding, of IN625, Song et al. [17] quantified the mechanical behavior of the stir zone in friction stir welded (FSW) joints and reported higher UTS values than cast, wrought, or liquid based additive manufactured data available in the open literature. While not an additive process, the FSW results by Song et al. illustrate the benefit of improved microstructure similar to the AFS-Deposition process.

1.2.3. Microstructure of Aluminum Alloy 2219

As with the IN625, AFS-Deposition is such a new process with no prior research on AFS AA2219. However, the FSW/P of AA2219, which are based on a similar solid state concept provide a starting point for understanding the microstructure influences that occur during solid state manufacturing. FSW has been a great option for welding similar and dissimilar metals presented in 1991 by TWI [10], and with research on AA2219 examining the effectiveness, optimal parameters and mechanical properties [8,11–13]. The microstructure of FSW has also been a point of interest among researchers, and specifically the stir zone (also known as nugget or DXZ) [8,14]. This is the area where the grains recrystallize, and refined grain sizes are observed [8,11,14]. The properties in this region are desirable, and for that reason a processing technique called FSP was also developed [15–18]. The FSP technique has also been a topic of interest, and a vast majority of research. In both FSW and FSP, as well as AFS-Deposition, the microstructure experiences dynamic recrystallization (DRX) [16–18]. There are two types of DRX in the literature, continuous DRX and discontinuous DRX. The difference between them is that in continuous DRX new grains are formed by a gradual increase in the misorientation between the subgrains [17,18]. In contrast, during discontinuous DRX, new grains with high angle boundaries are created. Previous research has demonstrated that it is common for

aluminum alloys to undergo dynamic recovery (DRV) during hot deformation [17–19]. DRV in aluminum is attributed to its high stacking fault energy which makes dislocation climb and cross slip easier [19,20]. Previous research by Su et al. [14–18,21] on AA7075 has shown that the FSW and FSP will experience different mechanism such as, discontinuous DRX, DRV, and continuous DRX at different stages of the microstructural evolution [14,17,18].

As previously mentioned, the AA2219 is a precipitation strengthened alloy with a variety of beneficial properties such as high strength-to-weight ratio, suitable weldability, resistance to stress corrosion cracking and superior properties at cryogenic temperatures [8,9]. The improved mechanical properties of AA2219 spread through a wide temperature range from -250 to 250 °C [22]. AA2219 has been successfully joined by different conventional joining processes, such as gas metal arc welding [23], gas tungsten arc welding [23], plasma arc welding [24], electron beam welding [yang 2000] and FSW [8,9,11,23,25].

However, since AFS-Deposition is a solid state additive process with similarities to FSW and FSP, the prior research discussed subsequently aides in elucidating mechanisms occurring during AFS-Deposition processing of AA2219. FSW is popular in different industries, such as aerospace and automotive, due to higher effective weld properties when compared against other welding techniques due to better retention of base material mechanical properties, less distortion and less weld defects [26,27]. Previous research on FSW of AA2219 has shown that the process results in a refined equiaxed microstructure in the weld zone, which improves strength and hardness [8,11,25,28]. However, all the aforementioned investigations have observed coarsening of the Al₂Cu θ particles. The θ particles are present in the base material, but smaller in size than in the weld zone. Li and Shen [28] attributed growth in the θ particles from a combined action of three different formation mechanisms: Aggregation Mechanism and Diffusion Mechanism I and

II. Additional research by Cao and Kou [12] concluded that there was no evidence of liquation in FSW 2219, since the welds only contain θ particles and no eutectic particles. Additionally, there is a wide range of reported sizes of the θ particles dependent on the FSW processing, going all the way up to 150 μm [9,11,12,28].

1.2.4. Mechanical Properties of Al Alloys

AA2219 in its O temper is reported to have a YS, UTS and elongation of 75 MPa, 175 MPa and 18 %, respectively [8]. In this investigation, the 2219-O is going to be the baseline for comparison since previous research on a variety of applications has been done on different tempers, and 2219-O is how the material is on its original state. As mentioned, there has not been any research in solid state additive manufacturing of AA2219 but preliminary data has identified that the microstructure of the AFS-Deposition process is similar to that of the stir zone in FSW. Due to a variety of end uses for the AA2219, multiple tempers have been investigated in the previous FSW research [8,9,11]. Tensile and microhardness testing on FSW butt welds of thick AA2219 plates have been investigated [8,23], in which the micro hardness testing showed a maximum value of 95 HV [8]. Specifically, prior research on butt FSW repair of thick plates of AA2219-T6 did testing on standard tensile specimens and reported tensile YS, UTS and elongation values of 345 MPa, 410 MPa and 15 %, respectively [11]. AA2219 additive manufactured by electron beam freeform (EBF) has been reported in the open literature [29–31], in which they observed that by varying the process parameters, the microstructure varied from fine equiaxed grain to dendritic. In addition, the researchers reported tensile mechanical properties of the as-deposited 2219 using EBF had a YS, UTS and elongation of 100 MPa, 275 MPa and 18%, respectively.

1.3 Objectives

The overall objective is to fundamentally understand the AFS-Deposition process effects on the resultant microstructure and mechanical properties for both an Inconel 625 (IN625) nickel-based superalloy and a precipitation hardened AA2219 to further improve the use of AFS-Deposition into commercial applications. For the AFS IN625 material, the tensile strain rate dependence is correlated to the as-deposited AFS microstructure. For the AFS AA2219, the sponsor provided more deposited material, so the as-deposited structure is correlated to the stress-state and strain rate dependence as a function of deposition orientation. These are important fundamental understandings since AFS-Deposition is a new technology with the process having significant growth opportunities for manufacturing and repair for the aerospace, transportation, and petro-chemical industries to name a few. The initial as-deposited microstructure is being studied using scanning electron microscopy (SEM) coupled with electron backscatter diffraction (EBSD) and Vickers microhardness for both materials. For the IN625, static (0.001/s) and dynamic (1500/s) longitudinal tensile test were performed. In the case of the AA2219, three directions, short transverse (build direction), long transverse and longitudinal, are being mechanically tested in compression and tension under static (0.001/s) and dynamic (1500/s) rates. For the AA2219, a physics-based model that includes microstructure based internal state variables for plasticity and damage is used to capture the stress state and strain rate behavior for AFS-Deposition component design and performance prediction to improve efficiency, quality and reduce production costs to generate new business opportunities.

1.3.1. Specific Objectives

- 1) Characterize the microstructure evolution and the static and dynamic mechanical properties of AFS Inconel 625.
- 2) Characterize the microstructure evolution and the static and dynamic mechanical properties of AFS AA 2219.
- 3) Perform an ISV model calibration of the AFS AA2219.

1.4. Chapter Preface

Chapter 2 focuses on the resultant microstructure and mechanical properties of AFS-Deposition Inconel 625 (IN625) nickel-based superalloy. In this chapter, significant EBSD analysis performed microstructural characterization to understand the grain morphology and size distribution along the build of the AFS-Deposition part. Mechanical properties of the material were evaluated in quasi-static (0.001/s) and high rate (1500/s) strain rates using servo hydraulic load frame and direct-tension Kolsky bar, respectively, to capture the mechanical properties as the strain rate is increased.

Chapter 3 presents the results on the as-deposited microstructure and mechanical properties of AFS-Deposition AA2219. Microstructural analysis was performed to understand the 3D microstructure, using optical microscopy, SEM, EBSD and TEM. In addition, hardness mapping along with tension and compression experiments determined the mechanical properties of the material. Furthermore, the tension and compression experiments were performed at quasi-static (0.001/s) and high rate (2500/s) to capture the material strain rate dependence. The compression and tensile experiments were performed in a various orientations of the build to verify any material anisotropy.

Chapter 4 is the calibration of the ISV plasticity-damage model of the AFS-Deposition AA2219. Further microstructural characterization was performed to capture all the microstructural constants needed for calibrating the model. Additional experiments, tension-followed-by-compression and compression-followed-by-tension, at different prestrain levels were performed to verify the Bauschinger effect of the material. The BE data and the QS tension and QS compression data were then further used as whole datasets to calibrate the model and obtain one set of constants that captures the material behavior and the stress-state asymmetry.

CHAPTER 2 MICROSTRUCTURES AND MECHANICAL BEHAVIOR OF INCONEL 625 FABRICATED BY SOLID-STATE ADDITIVE MANUFACTURING

2.1. Introduction

Aeronautic, aerospace, marine and chemical are just a few of the many industries interested in additively manufactured metals with specific properties tailored for highly specialized operating conditions [1,6,32,33]. One specific property needed in many of these industrial applications is high temperature mechanical stability, including strength and ductility, that is found in superalloys [34–36]. One of these superalloys that has gained wide industrial usage is IN625, a nickel-based superalloy [32]; This alloy has been found to provide high strength and good ductility at temperatures up over 1000 °C, as well as the added benefit of oxidation resistance in aggressive environments [2]. The thermo-mechanical Solid State Additive Manufacturing (SSAM) process, Additive Friction Stir (AFS), developed and patented by Aeroprobe Corporation [37] provides a new method for additive manufacturing fully-dense IN625 components with unique benefits for coating, joining, repairing and net shaping applications with exceptional mechanical properties.

Alternative methods for producing IN625 through additive manufacturing have also been reported in the open literature. Some of these alternative methods include pulsed plasma arc deposition (PPAD) [6], laser aided direct metal deposition (DMD) [2], and laser rapid

manufacturing (LRM) [4,38]. All of the aforementioned 3D printing techniques [2,4,6,38–42] report in their research a columnar dendritic microstructure dependent on the build direction. Additionally, in these additive processes, the reported values of yield strength (YS) and ultimate tensile strength (UTS) were superior to those of as cast IN625 [43], but with similar properties to wrought IN625 [44]. Lastly, Song et al. [3] performed tensile testing on specimens extracted from the stir zone of FSW IN625 and reported higher UTS values than cast, wrought, or liquid based additive manufactured data available in the open literature.

The concept of AFS is built upon the inherent benefits of friction stir welding/processing (FSW/P) in that a robust metallurgical bond is created during solid state processing [45,46]. The AFS process feeds metal powder or solid rod through a non-consumable rotating cylindrical tool generating heat and plastically deforming the feedstock material through controlled pressure from the tool as successive layers are built upon a substrate. As each layer is added, the tool height increases to accommodate the subsequent material deposition, forcing the material into the previous layer, thus creating a strong metallurgical bond between the layers. During this process advantages such as: grain refinement, homogenization, and reduction of porosity is established similarly to traditional friction stir processing by tool force and rotation combined with transverse tool movement. Since this is a solid-state process, AFS eliminates common problems such as porosity, hot cracking, elemental segregation and dilution associated with fusion-based techniques. Other impacts on material properties of the build layers such as grain refinement are a benefit of the process. Since deposited materials remain below their melting point, distortion in manufactured parts and substrates are lower when compared to other fusion-based processes. The process temperature is expected to be similar to the peak temperature that exists in the nugget zone of friction stir welding/processing, which is $0.6 - 0.9 T_m$, where T_m is

the melting point of the material [45]. AFS is highly scalable with deposition rates greater than 80 cm³/hr for IN625, which allows for AFS to coat and repair large parts or build fully-dense additive components.

FSW has gained popularity in different industries due to the higher effective weld mechanical properties that may be obtained when compared to fusion welds. This increase in FSW research aided in elucidating some of the microstructural evolution and mechanical behavior phenomenon that may occur during AFS processed Inconel alloys [26,46,47]. Specifically, research by Song and Nakata on FSW IN625 found that the process of FSW recrystallized the grains, thereby improving both the hardness and strength [3]. Similar research on FSW of Inconel 600 also showed benefits of grain refinement to improve the mechanical properties of the weld [48]. However, both investigations observed a decrease in the elongation-to-failure compared to the base material as grain size was refined. Song and Nakata identified grain diameters in the IN625 base material to be between 5 to 15 μm , with an average size of 10.3 μm , whereas in the stir zone the grain diameter was reduced to between 1.3 to 3 μm , with an average size of 2.1 μm [3] exhibiting an equiaxed grain morphology.

In this manuscript, the microstructures and resultant mechanical properties produced in IN625 by the AFS process is reported for the first time. Electron Backscatter Diffraction (EBSD) is used to quantitatively characterize the microstructure of IN625 produced by AFS. The tensile mechanical properties of the AFS-produced material are measured at both quasi-static and high strain rates, which are correlated to the microstructural evolution using a novel correlation of plasma focus ion beam (FIB) milling and EBSD along the tensile crack path.

2.2. Materials and Methods

Aeroprobe Corporation provided AFS fabricated samples by pushing a solid IN625 rod through a hollow tool to deposit the material onto a HY80 [49] substrate. During the AFS process, the solid filler material was added and heat generated by friction between the filler material and the tool shoulder under hydrostatic pressure and the substrate plastically deformed both filler and substrate as they were stirred together to metallurgically bond the material to the substrate and the successive layers of IN625 as depicted in Figure 2-1. The average chemical composition of the rod-stock material is shown in Table 2-1. For the samples in this study, the AFS IN625 manufactured part consisted of 5 layers that were approximately 0.5 mm in thickness per layer.

Table 2-1. Chemical composition of IN625.

Elements	Ni	Cr	Mo	Mn	Si	Al	C	Cu	P	S
Percentage	61.0	22.0	8.22	0.37	0.27	0.08	0.07	0.03	0.00	<0.00
	0	1							8	1

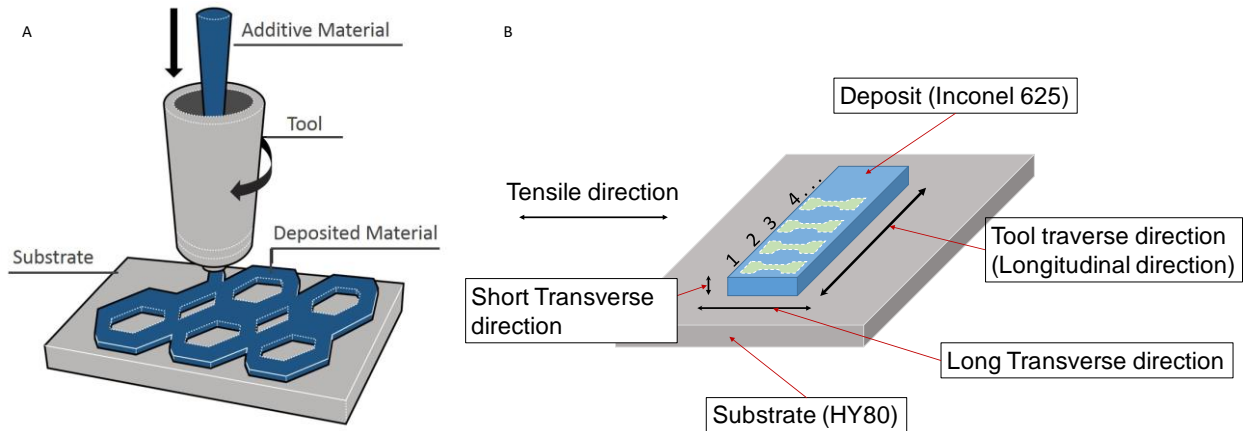


Figure 2-1. (A) SSAM process starting with solid filler material extruded through a hollow tool. (B) Schematic of the AFS deposition of IN625 and orientation of the tensile specimens.

After deposition, samples obtained from Aeroprobe were prepared for microstructural characterization by mounting them in conductive mounting media, grinding down to a 1200 grit SiC paper and then step-wise polishing down to a final polish with a 0.05 μ m colloidal silica solution.

A Tescan Lyra FIB-FESEM equipped with an EDAX Hikari Super EBSD camera and an Octane Elite Silicon Drift Detector performed the EBSD, electron dispersive X-ray spectroscopy (EDX) and fractography of the as-deposited and fractured samples, respectively. The EBSD scans were performed at the same magnification along the build direction over an area of approximately 40 x 40 μ m, with a step size of 0.1 μ m for the maps in the individual layers and 0.08 μ m for the maps at the interfaces between layers. The scans were performed at 20KV and beam current of 5.5nA. Images were taken in the three different directions, as shown in Figure 4A, to analyze the grain size and geometry to understand the microstructure evolution in the build direction, long transverse direction, and short transverse direction in the specimens. The EBSD data was post-processed using the grain dilation algorithm in the EDAX software with settings of a minimum grain size of 2 pixels and requiring that a grain must contain multiple rows of pixels. The grain diameter was determined measuring the area of each grain using the OIM software, and then calculating the average grain diameter assuming circular grain morphology.

For the tensile specimens, wire EDM was used to machine flat dogbones with the tensile axis oriented parallel to the long transverse direction of the build. The same specimen geometry (Figure 2-2) with a gauge length of 4.5mm, width of 2.0mm and thickness of 1.5mm was used for testing at both the quasi-static (QS) and high rate (HR) strain rates for strain-to-failure comparison purposes as implemented in previous studies [50,51].

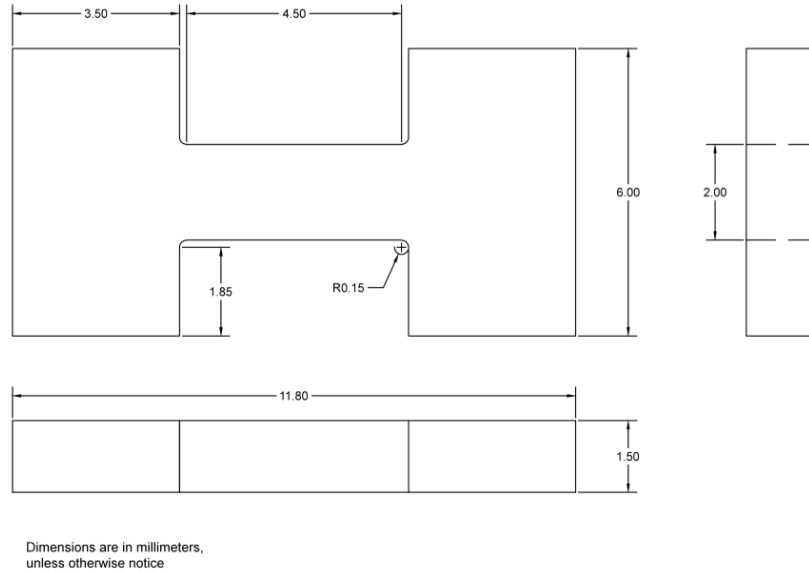


Figure 2-2. Tensile specimen geometry used for both quasi-static (0.001/s) and high rate (1500/s).

A servo hydraulic MTS landmark 370 load frame equipped with a 100 KN load cell performed the QS tensile experiments at a strain rate of 0.001/s. The load-displacement data from the MTS machine was converted to engineering stress-strain. The MTS strain values were compared against video strain data. Using an in-house Matlab routine, the video strain data calculated was using a normalized cross-correlation technique (normxcorr2) [52,53]. A direct-tension Kolsky bar made of 350-maraging steel with 12.7 mm diameter for the striker, incident and transmitted bars performed the dynamic tensile experiments at a strain rate of 1500/s. A Matlab subroutine processed the high rate strain gage data obtained from semiconductor strain gages[54]. All the QS and HR experiments were performed in triplicate at ambient temperature.

2.3 Results and Discussion

Optical microscopy was used to compare the as-received microstructure to the as-built microstructure. The as-received material grain size of the solid filler material provided by the

manufacturer was reported to have an average grain size of approximately 30 μm . Figure 2-3A and 2-3B shows a comparison between the microstructure of the as-received material and the as-built AFS material, respectively. Figure 2-3B displays significant grain refinement for the AFS processed as-built material when compared to that as-received microstructure. Quantification of grain size for the as-built IN625 was quantified with EBSD and is discussed subsequently.

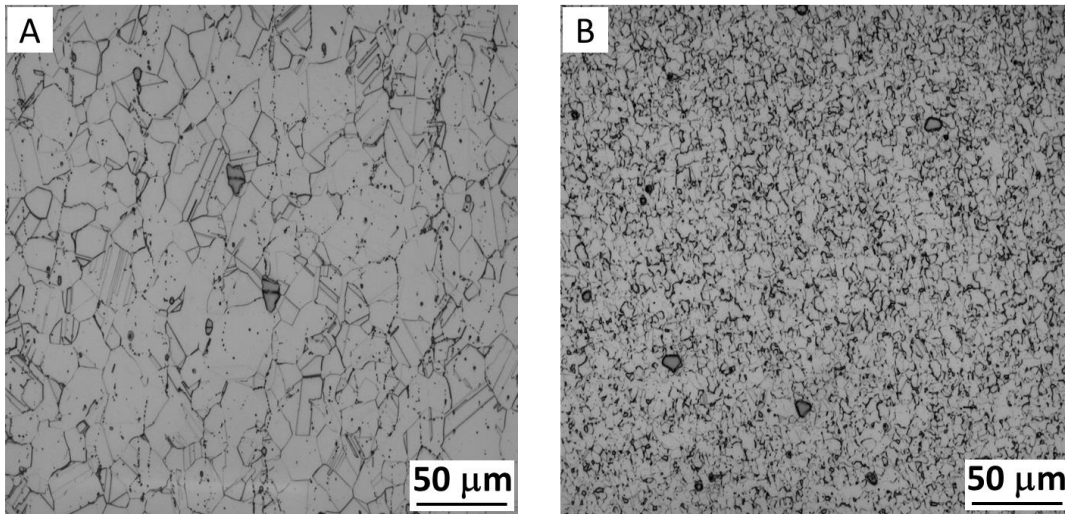


Figure 2-3. Optical micrograph comparing the microstructure between (A) as-received IN625 filler material and (B) as-built AFS IN625.

EBSD performed along the build direction (Figure 2-4) provided a thorough understanding of the initial state microstructure of the tensile specimens. In Figure 2-4A, the orientation of the EBSD scans in relation to a representative tensile specimen are shown since EBSD scans were performed after receiving the machined specimens from Aeroprobe. The EBSD inverse pole figure (IPF) maps in Figure 4B correlate to the locations depicted in Figure 2-4A. The EBSD identified fine equiaxed grain (0.5 μm weighted average, with a 1.3 μm max) structures with even finer grain structures (0.26 μm) forming at the layer interfaces. Figure 2-4C

correlates the average grain diameter and the number of grains identified by EBSD for the locations in Figure 2-4A and 2-4B. Figure 2-5 provides a higher detailed analysis of three locations identified in Figure 2-4C. This analysis was performed for all locations, but since the behavior was similar, only three locations are shown here for brevity. Figure 2-5A, 2-5D, and 2-5G are the magnified Euler EBSD IPF map shown previously in Figure 4B. Grain boundary maps in Figure 2-5B, 2-5E, and 2-5H show a dominant fraction of high angle grain boundaries. The EBSD also observed that the fraction of high angle boundary increases from 0.82, 0.84 and 0.91 for locations 1, 2, and 3, respectively. Also, the measured grain size decreases toward the interface region (Figure 2-5B, 2-5E, and 2-5H, respectively). Grain reference orientation deviation (GROD) maps (Figure 2-5C, 2-5F, and 2-5I) show that the amount of intragranular misorientation decreases from the center of a layer towards a layer-layer-interface, GROD maps will show low levels of intragranular misorientation (~0.5 degrees) for crystals that are undeformed, while intragranular misorientation values of 1.5 degrees or larger will be observed in plastically deformed crystals [55]. In Figure 2-5C, many grains have significant levels of intragranular misorientation, indicating large levels of geometrically necessary dislocations. The microstructure in Figure 5F still shows these deformed gains, albeit with fewer grains than in Figure 2-5C. In the near-interface region (Figure 2-5I), most grains are blue in color and are likely recrystallized. There are isolated grains with high levels of intragranular misorientation.

The optical microscopy and EBSD data strongly suggest that dynamic recrystallization (DRX) is taking place in the stirred region of the material during AFS. The significant reduction in grain size observed both in the optical microscopy (Figure 2-3) and EBSD data (Figures 2-4 and 2-5) is the first point indicating recrystallization. In addition, the finer grains have low levels of intragranular misorientation, as evidenced by the GROD maps (Figures 2-5C, 2-5F, and 2-5I).

Recrystallized grains should display lower levels of intergranular misorientation due to their lower dislocation densities. While the temperature during AFS was not directly measured, it is generally thought that friction stir processes increase the temperature of the material in the stir zone to temperatures between 60-90% of the melting point [45], high enough to produce recrystallization during the intense shear deformation of the AFS process. The grain boundary maps in (Figures 2-5B, 2-5E, and 2-5H) provide further information about the possible nature of the recrystallization process. As described by Doherty et al. [20], DRX is a process in which new grain structures are produced in a deformed material via the creation and migration of grain boundaries driven by the stored energy of deformation. Furthermore, dynamic recrystallization happens during the deformation process. The presence of a significant fraction of low angle boundaries (red lines in Figures 2-5B, 2-5E, and 2-5H) in an otherwise recrystallized microstructure suggests that new grain boundaries are being formed during the dynamic deformation process and that the migration of these boundaries will produce DRX. Humphreys distinguishes between a discontinuous recrystallization process in which the grain nucleation and growth will occur heterogeneously throughout the material and a continuous process in which grain nucleation and growth happens uniformly and gradually; and as such, there is no identifiable nucleation and growth stages [56]. Baker et al., uses the term “continuous dynamic recrystallization” as defined by Humphreys, to describe the stir zone microstructures produced by FSW in ODS steels [57]. Similar, DRX microstructures have been observed for FSW of AA7075 aluminum alloys as well [14].

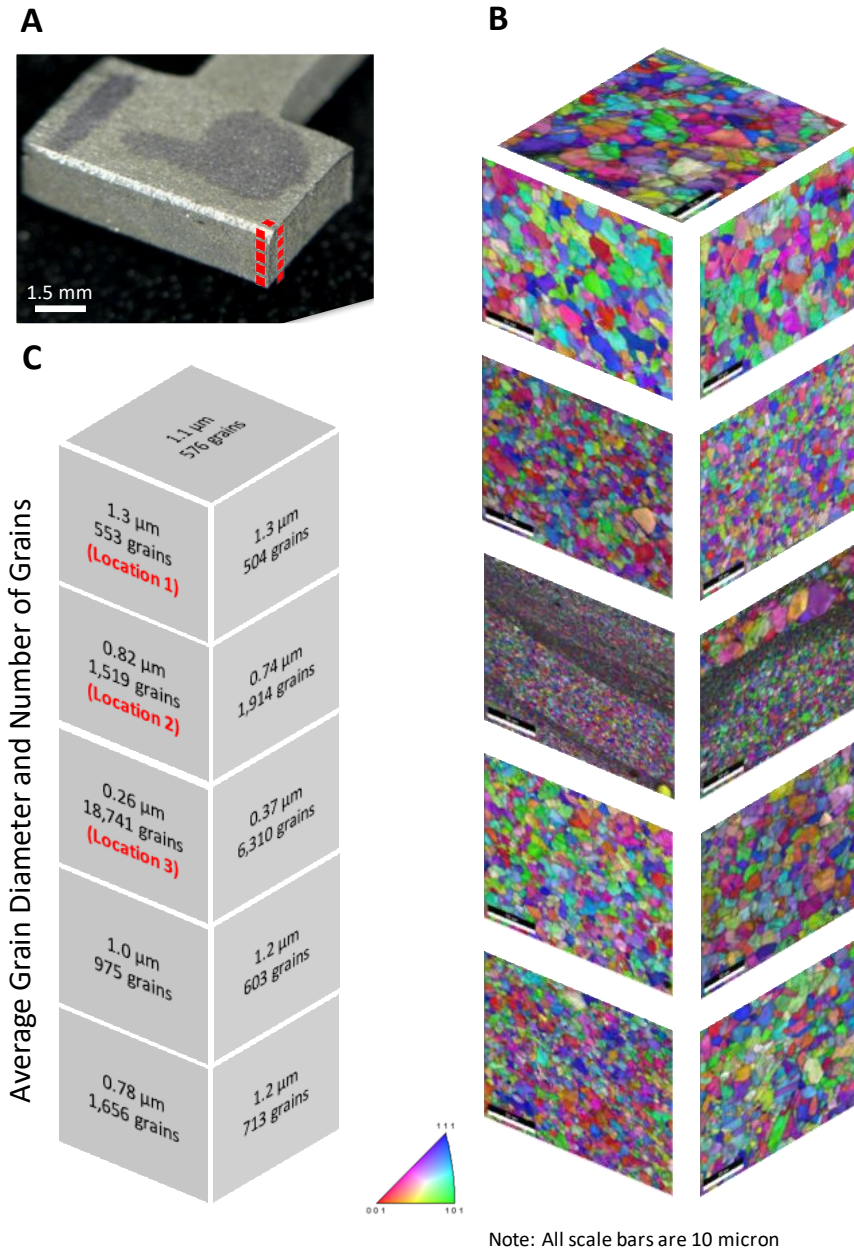


Figure 2-4. (A) Euler EBSD maps representative location on sample, (B) Euler EBSD maps of 5 locations along build direction, all images are at the same magnification and same location in the corresponding axis, (C) Average grain size and number of grains (location correlates with the EBSD map locations in A and B).

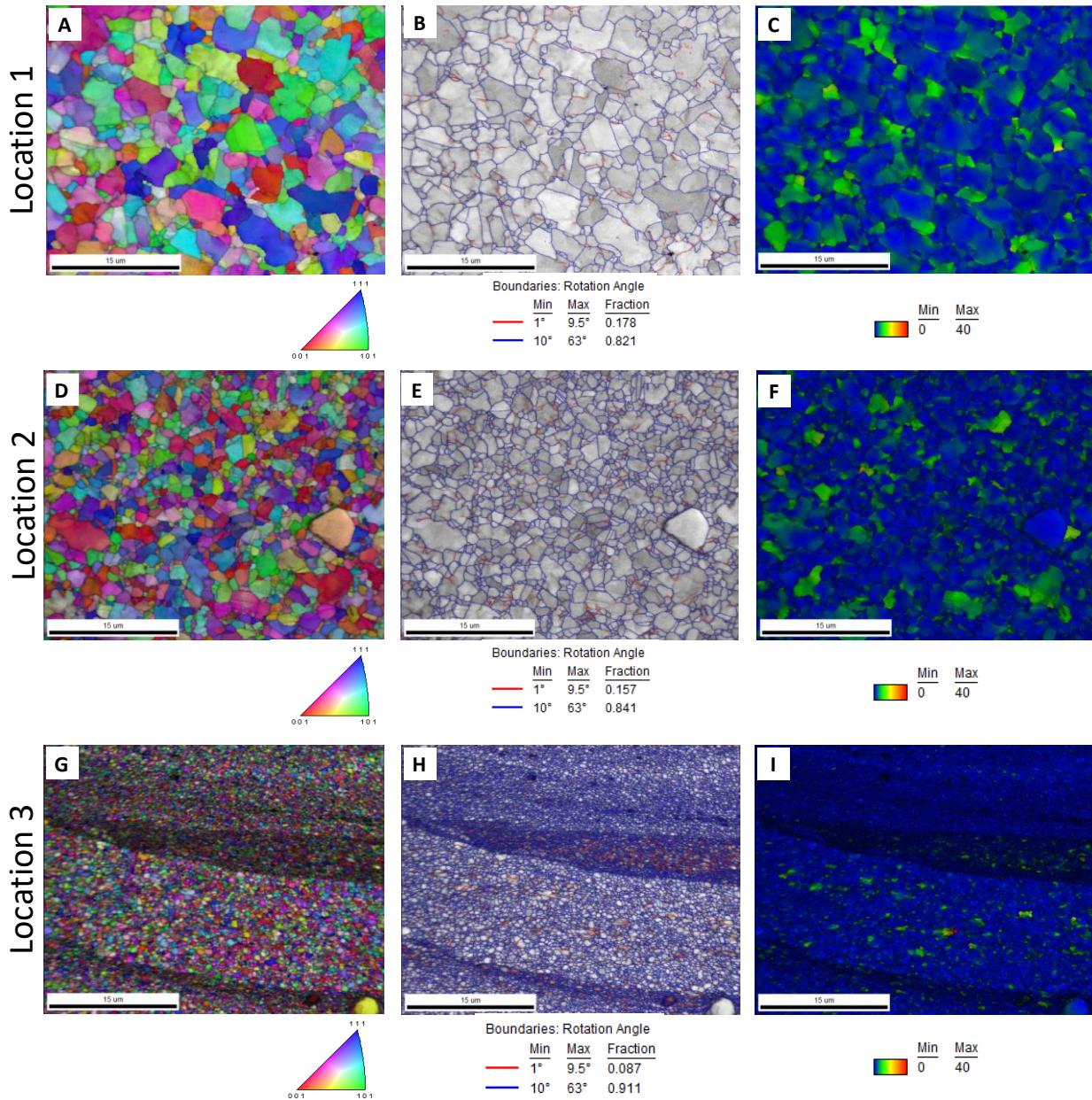


Figure 2-5. (A, D, G) Euler EBSD map representative of the middle location. (B, E, H) Boundary rotation map showing the dominant high angle boundary. (C, F, I) Grain reference orientation deviation map.

Figure 2-6 plots the average QS and HR tensile behavior of the AFS material in the long transverse direction with associated error bands corresponding to the maximum and minimum experimental values. The mechanical behavior of the QS tensile specimens produced an average yield strength (YS) of 730 MPa, an ultimate tensile strength (UTS) of 1072 MPa, and a strain to

failure of 0.32. The specimens exhibited strain hardening and softening after yielding, which was observed by elongation in the gage section. The tensile specimens failed in ductile fashion with the fracture surface at 45° to the tensile axis, as would be expected for the maximum shear strain plane (Figure 2-7A-D). The QS results for the additive components compare similarly to previous research on FSW by Song and Nakata [3] on tensile testing of FSW IN625 samples. Song and Nakata tested specimens of the joint and in the stir zone and their results showed a UTS of 1019 MPa and 1152 MPa, respectively, and an elongation of 34% and 35% respectively in the two different zones [3].

The HR specimens achieved a higher average YS, UTS and elongation to fracture at 1587 MPa, 1592 MPa and 0.34, respectively (Figure 2-6). The HR results depicted an approximate 200 MPa increase along the curve of the HR data as seen in Figure 2-6. The HR samples also exhibited hardening and softening after an initial peak and failed in a 45° type of fracture aligning with the maximum shear strain plane as seen Figures 2-8A-D.

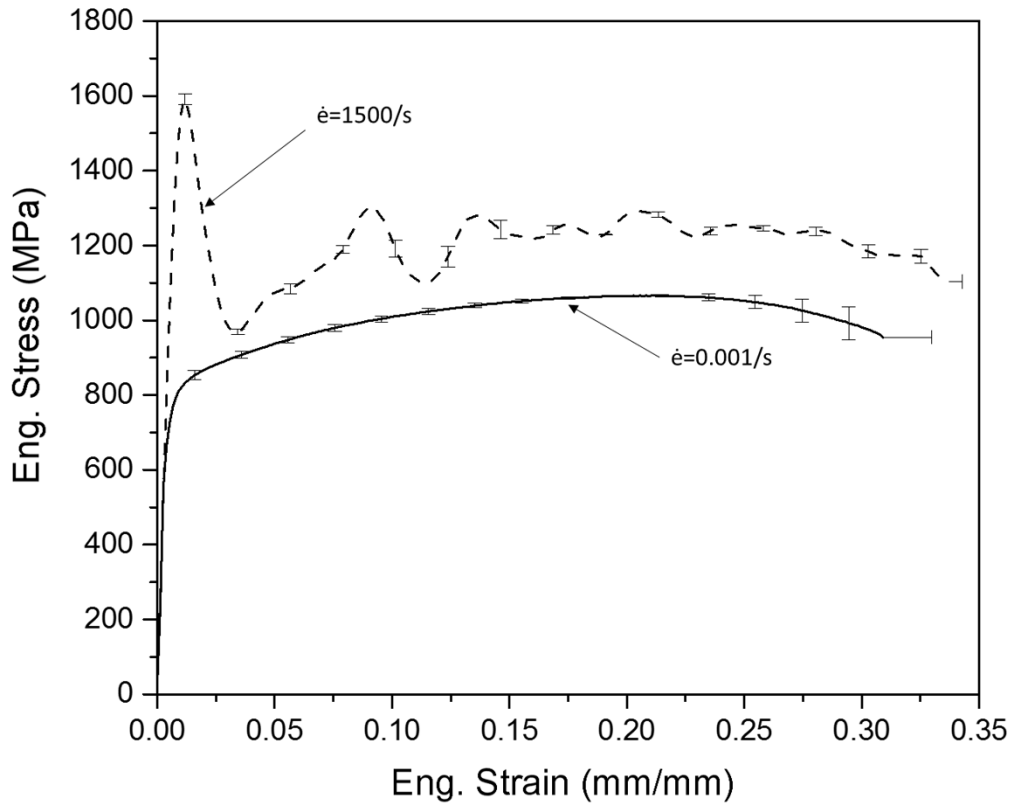


Figure 2-6. Tensile results comparing the quasi-static (0.001/s) to the high rate (1500/s). The quasi-static achieved a YS of 730 MPa, UTS of 1072 MPa and strain to failure of 0.32. The high rate high rate achieved a YS of 1587 MPa, UTS of 1592 MPa and a strain to failure of 0.34.

Interestingly, the AFS process resulted in higher YS and UTS for IN625 when compared to fusion-based additive manufacturing, cast and wrought data reported in the literature for IN625 (Table 2-2). A very different grain morphology and microstructure between the AFS IN625 and other additive manufacturing processed IN625 is a likely contributor to the difference between the mechanical properties reported. Table 2-2 summarized that the AFS process results in equiaxed grains in the three directions (Figure 2-3), whereas the other additive processes report mostly a columnar preferred orientation. The strain to failure was not directly compared to published literature data since this study used a subscale specimen for both QS and HR experiments instead of a larger ASTM E8 tensile coupon, but a column of strain to failure is

provided for reference in Table 2-2. Since the AFS IN625 outperformed the IN625 manufactured by other methods, a comparison to cast, wrought, and SLM IN718 was also warranted in Table 2-2. The comparison of the results show that the YS of AFS IN625 is not as high as any of the IN718 reported in Table 2-2, but the UTS is similar to that of cast IN718. Suggesting that an investigation into AFS processed IN718 may result in some remarkable properties for the end-users.

Table 2-2. Comparison of IN625 microstructure, YS and UTS of different manufacturing processes.

Condition	Grain Morphology	YS (MPa)	UTS (MPa)	ef (%)
Cast IN625 [43]	-	350	710	48
Wrought IN625 [44],[49]	-	490	965	30-50
AFS IN625	Equiaxed	730	1072	32
FSW IN625 (stir zone specimen) [3]	Equiaxed	-	1152	35
Plasma Pulsed Arc Deposition (PPAD) IN625 ^ [6]	Columnar Dendrites	438	721	49
Laser Rapid Manufacturing (LRM) IN625 ^ [4]	Columnar / Dendrites	572	925	49
LRM IN625 ^ [38]	Columnar / Dendrites	518	797	31
LRM IN625 ^ [39]	Columnar / Dendrites	540	690	36
Laser Aided Direct Metal Deposition (DMD) IN625 ^ [2]	Columnar Dendrites	-	-	-
Laser Melted Deposition (LMD) IN625 ^ [40]	Cellular / Dendrites	656	1000	24
Electron Beam Melting (EBM) IN625 ^ [41]	Columnar	410	750	44
Selective Laser Melting (SLM) IN625 ^ [42]	Dendritic	380	900	58
Cast IN718 [43]	-	915	1090	11
Wrought IN718 [44]	-	1185	1435	21
SLM IN718 ^ [58]	Dendritic	889-907	1137-1148	19.2-25.9

Notes:

^Data reported from the optimal orientation

Optical micrographs of the fracture surfaces for both the QS and HR specimens depicted in Figure 2-7A and 2-8A respectively, indicate alignment along the maximum shear strain plane. Fractography images from the SEM for a representative QS specimen are shown with increasing

magnification in Figures 2-7B, 2-7C, and 2-7D, respectively. Similarly, SEM fractography images for a representative HR specimen are shown with increasing magnification in Figures 2-8B, 2-8C, and 2-8D, respectively. In both QS and HR specimens, microvoids are observed on the fracture surfaces in addition to localized delamination of individual layers identified in specific areas of the fracture surface.

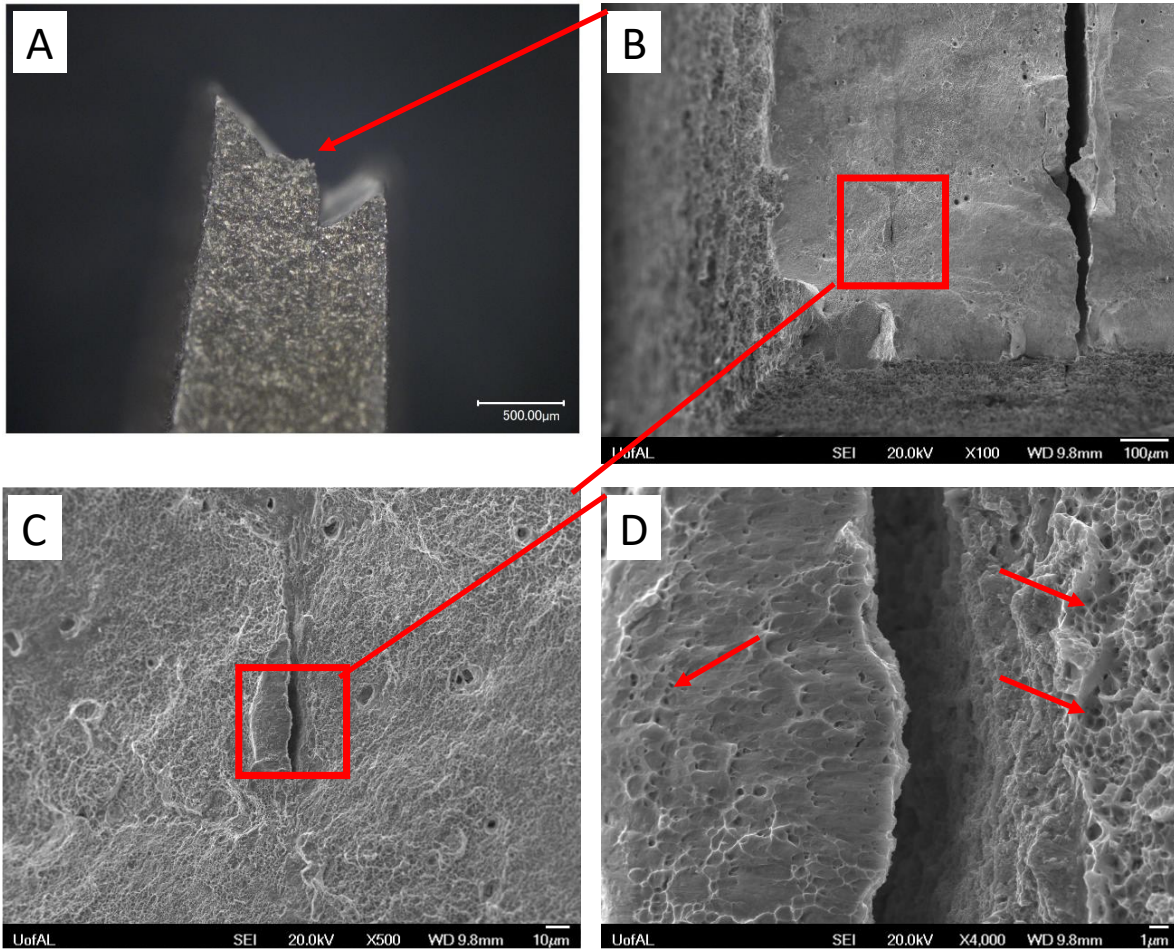


Figure 2-7. Fractography of the QS (strain rate of 0.001/s) tensile specimen tested to failure. Image A is an optical micrograph of the fracture surface of QS specimen (500 micron scale bars) aligned with the maximum shear strain plane. Images 2-7B, 2-7C and 2-7D (scale bars are 100, 10 and 1 micron, respectively) are SEM images with increasing magnification with arrows pointing to microvoids in 2-7D.

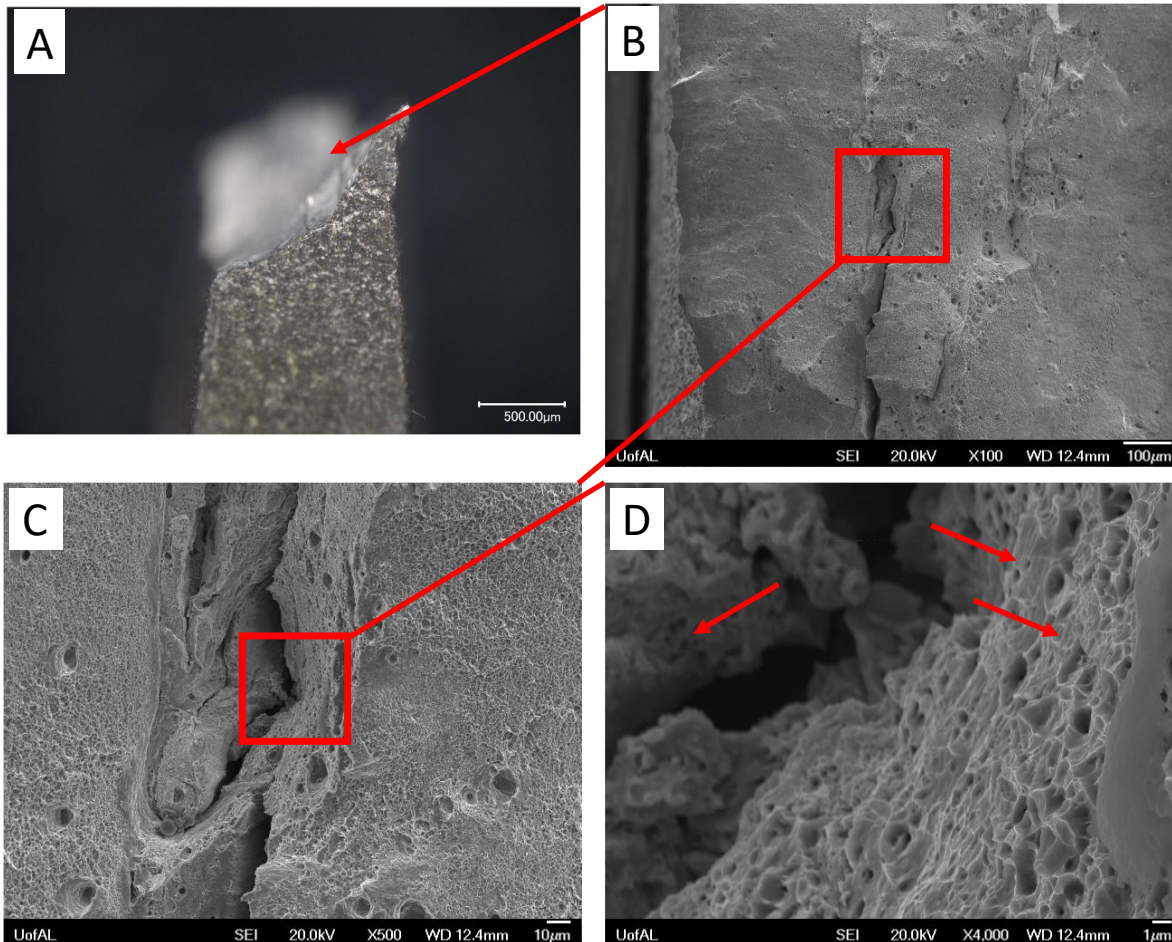


Figure 2-8. Fractography of the HR (strain rate of 1500/s) tensile specimen tested to failure. A is an optical micrograph of the fracture surface of HR specimen (500 micron scale bars) aligned with the maximum shear strain plane. Images 2-8B, 2-8C and 2-8D (scale bars are 100, 10 and 1 micron, respectively) are SEM images at increasing magnifications with arrows pointing to the microvoids in 2-8D.

In Figure 2-7A, the SEM observed a crack that propagated parallel to the loading direction. Further analysis was performed to further elucidate the microstructure relating to that fracture morphology. Using a plasma focused ion beam (PFIB), the specimen was prepared for EBSD (Figure 2-9A). The same EBSD parameters from the interface EBSD maps were used. Figure 2-9B is an SEM image of the area analyzed with EBSD. In the IPF EBSD map of Figure 2-9C, a DRX zone next to the crack is identified. High angle boundaries dominate the area closer

to the crack (Figure 2-9D), and deformation is also observed outside that DRX zone as seen in Figure 2-9E. The crack is intergranular, propagating through the DRX grains as clearly shown in Figure 2-9F.

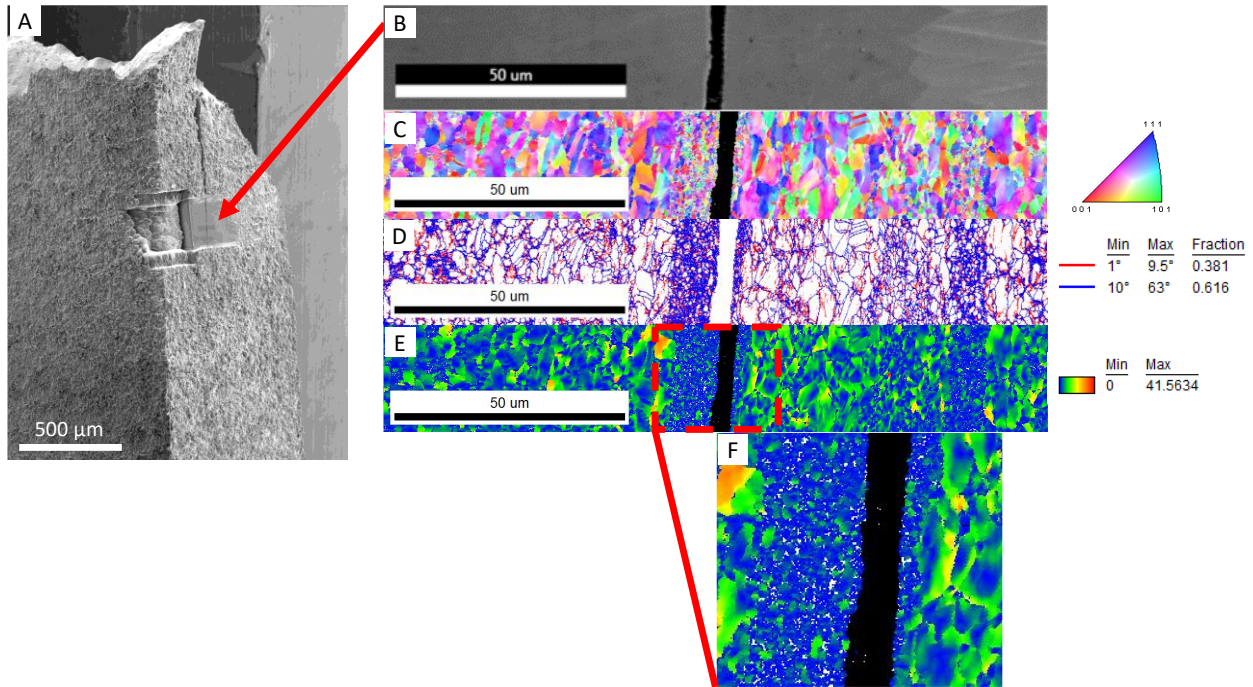


Figure 2-9. (A) SEM image of tensile specimen with crack parallel to loading direction (other side of Figure 2-6A). (B) SEM image of area analyzed with EBSD. (C) Euler EBSD map representative of the middle location. (D) Boundary rotation map showing the dominant high angle boundary. (E) Grain reference orientation deviation map. (F) Close-up of the crack region in the grain reference orientation deviation map.

2.4. Conclusions

This manuscript is the first to detail the microstructural evolution and mechanical properties of solid-state, additively manufactured IN625 using a thermo-mechanical AFS process. The EBSD results detailed a significantly refined, equiaxed grain structure, which is likely produced by continuous DRX during AFS. The recrystallized microstructure is localized to interface layers that separate macroscale layers formed by repeated passes of the AFS tool.

EBSD observed grains as fine as 0.27 microns in these layer interface regions, while the average grain size was approximately 1 micron in the other regions of the deposited layers. The strain rate dependence of these of these fine-grained materials were examined at both QS (0.001/s) and HR (1500/s) strain rates using servo hydraulic and a direct tension-Kolsky bar, respectively, exhibiting both increases in yield and ultimate tensile strengths as strain rate increased.

Additionally, when compared to other processing methods for IN625, the AFS results displayed comparable values to the reported FSW UTS data, but significantly higher YS and UTS than the other cast, wrought, or fusion-based AM data.

CHAPTER 3
INFLUENCE OF STRESS-STATE AND STRAIN RATE DEPENDENCE OF SOLID STATE
ADDITIVE MANUFACTURED AA2219

3.1. Introduction

Additive Friction Stir (AFS) is novel solid-state additive manufacturing (AM) process, which is being reported for the first time on AFS processed aluminum alloys, specifically Aluminum Alloy (AA) 2219. The AFS process shares some similarities to friction stir welding and processing (FSW/P), but is significantly different in the aspect that filler material flows through a rotating hollow tool with the filler material being deposited onto a substrate while remaining completely in the solid state. As described in previous research by Rivera *et al.* [Citation here] on AFS processed IN625, the AFS-Deposition process can either feed from solid or metal powder material, pushing it through a non-consumable rotating cylindrical tool. This will generate heat and plastically deform the feedstock material under controlled pressure from the tool while layers are built upon a substrate. Once a layer is added, the tool height increases to begin the deposition for the next layer, creating a strong metallurgical bond between layers. Some advantages of this process are grain refinement, homogenization, and reduction of porosity. During the process, temperatures similar to those in the weld nugget zone (WNZ) of FSW, which are between $0.6 - 0.9 T_m$, where T_m is the melting point of the material [45]. Being a highly scalable process, with deposition rates for AA over $1000 \text{ cm}^3/\text{hr}$, AFS-Deposition allows for repairing, coating, and/or building fully-dense materials.

Unique features of the AA2219 is that the material is a precipitation strengthened alloy with a variety of beneficial properties such as high strength-to-weight ratio, suitable weldability, resistance to stress corrosion cracking and superior properties at cryogenic temperatures [8,9]. The improved mechanical properties of AA2219 spread through a wide temperature range from -250 to 250 °C [22]. AA2219 has been successfully joined by different conventional joining processes, such as gas metal arc welding [23], gas tungsten arc welding [23], plasma arc welding [24], and FSW [8,9,11,23,25].

Little AM research on AA2219 has been reported to-date. However, AA2219 electron beam freeform (EBF) AM has been reported in the open literature [29–31], in which they observed that by varying the process parameters, the microstructure varied from fine equiaxed grains to dendritic. In addition, the researchers reported tensile mechanical properties of the as-deposited AA2219 using EBF had a YS, UTS and elongation of 100 MPa, 275 MPa and 18%, respectively.

FSW of AA2219, which is based on a similar solid-state concept provide a starting point for understanding the microstructure evolution that occurs during solid-state processing. FSW has been a useful option for welding similar and dissimilar metals that were originally presented in 1991 by TWI [10], and with prior FSW research on AA2219 examining the effectiveness, optimal parameters and mechanical properties [8,11–13]. FSW is popular in multiple industries, such as aerospace and automotive, due to higher effective weld properties when compared against other welding techniques due to better retention of base material mechanical properties, less distortion and less weld defects [26,27]. The microstructure of FSW components has also been a point of interest among researchers with specific emphasis on the stir zone (SZ), also known as the nugget [8,14]. This is the area where the grains recrystallize, and grain refinement

is observed [8,11,14]. The properties in this region are desirable, and for that reason a processing technique called FSP was also developed [15–18]. The FSP technique has also been a topic of interest experiencing significant research [15,17,18,21]. In both FSW and FSP, as well as AFS-Deposition, the microstructure may experience dynamic recrystallization (DRX) [16–18]. There are two types of DRX in the literature, continuous DRX and discontinuous DRX. The difference between them is that in continuous DRX new grains are formed by a gradual increase in the misorientation between the subgrains [17,18]. Under discontinuous DRX, grains with high angle grain boundaries form through dynamic nucleation and growth from a previously deformed microstructure. Previous research has demonstrated that it is common for aluminum alloys to undergo dynamic recovery (DRV) during hot deformation [17,18]. Additionally, research by Su *et al.* [14–18,21] on AA7075 has shown that the FSW and FSP will experience different mechanism such as, discontinuous DRX, DRV, and continuous DRX at different stages of the microstructural evolution [14,17,18].

Due to a variety of end uses for AA2219, the mechanical properties of multiple tempers have been investigated in previous FSW research [8,9,11]. Tensile and microhardness testing on FSW butt welds of thick AA2219 plates have been investigated previously [8,23] with microhardness testing showing a maximum value of 95 HV [8]. Additional research on FSW butt welds of AA2219-T6 thick plates with standard tensile specimens reporting tensile YS, UTS and elongation values of 345 MPa, 410 MPa and 15 %, respectively [11].

Additionally, as AFS-Deposition is a solid-state additive process with similarities to FSW and FSP, the prior FSW research discussed subsequently aides in elucidating mechanisms occurring during AFS-Deposition of AA2219. Specifically at the microstructural level, prior FSW AA2219 research has shown a refined equiaxed microstructure in the weld zone is

attainable, which improves strength and hardness [8,11,25,28]. Additionally, the aforementioned investigations have observed coarsening of the Al₂Cu θ particles. Where the θ particles are present in the base material, but smaller in size than in the weld zone. Li and Shen [28] attributed growth of the θ particles from a combined action of three different formation mechanisms: Aggregation Mechanism and Diffusion Mechanism I and II. Furthermore, research by Cao and Kou [12] concluded that there was no evidence of liquation in FSW AA2219, since the welds only contain θ particles and no eutectic particles. Subsequently, there is a wide range of reported sizes of the θ particles dependent on the FSW processing parameters, with sizes reaching up to 150 μm [9,11,12,28]. Previous research by Kang *et al.* [59] performed Transmission Electron Microscopy (TEM) in FSW of AA2219-T8, where they found θ' precipitates in the base material and only θ phase precipitates in the WNZ. In prior studies [59,60], the researchers saw an abnormal agglomeration of θ particles in the WNZ, which they concluded that this formation of particles was related to piling up, blocking and extrusion of the normal θ particles during the metal plastic flow.

This is the first manuscript to report the microstructure and resultant mechanical properties of AA2219 produced by the AFS-Deposition process. Electron Backscatter Diffraction (EBSD) and TEM are used to quantitatively characterize the microstructure of AFS-Deposited AA2219. Mechanical properties in tension and compression in quasi-static and high rates are reported.

3.2. Materials and Methods

Aeroprobe Corporation, who created and patented this technology, provided AFS-Deposition fabricated samples by pushing a solid AA2219-T851 rod through a hollow tool to

deposit the material onto a AA2219-T851 plate substrate. During the AFS-Deposition process, the solid filler material was added and heat generated by friction between the filler material and the tool shoulder under hydrostatic pressure and the substrate plastically deformed both filler and substrate as they were stirred together to metallurgically bond the material to the substrate and the successive layers of AA219 as depicted in Figure 3-1. The average chemical composition of the rod-stock material is shown in Table 3-1. In this study, 100 mm long AFS AA2219 depositions consisted of 6 layers that were approximately 1 mm in thickness per layer. From this point on, the build direction will be referred to as BD, the transverse direction as TD, and the longitudinal direction as LD.

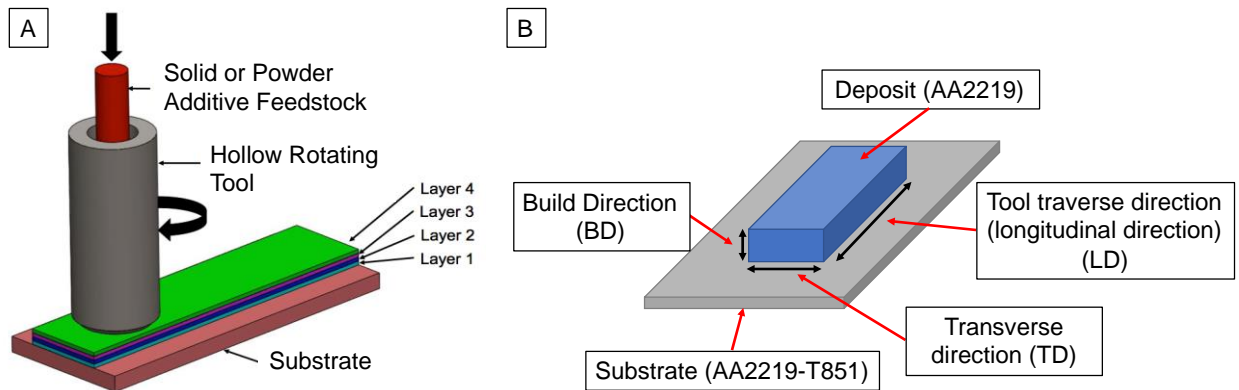


Figure 3-2. (A) SSAM process with solid filler material extruded through a hollow tool. (B) Schematic of the AFS deposition of AA2219 identifying the longitudinal, transverse and build directions.

Table 3-1. Chemical composition of AA2219 [61].

Elements	Al	Cu	Mn	Ti	V	Zr
Percentage	93.0	6.3	0.30	0.06	0.10	0.18
	6					

A wire EDM milled flat dogbone sub-compact tensile specimens with a geometry previously implemented for both high strain rate (HR) and quasi-static (QS) tensile experiments

on cast, wrought, and AM alloys [50,62,63]. The flat dogbones had a gauge length of 4.5mm, width of 2.0mm and thickness of 1.5mm (Chapter 2). The tensile specimens were machined from the bottom, middle and top of the build in the longitudinal direction (LD) and transverse direction (TD). An EDM also machined the compression specimens with a diameter of 6mm and a height of 6mm. The compression specimens were machined from the build direction (BD), TD and LD orientations to examine directional dependence of mechanical properties in the specimens (see Figure 3-9). As a first investigation, cross-sections were taken from the beginning, middle and end of the as-received deposition (see Figure 3-10) to quantify spatial dependence of the initial microstructure and Vickers microhardness in the deposition. For microstructural characterization, the three cross-sections were stepwise polished using an aqueous lubricant down to a 1200 grit SiC paper, then polished using 1 and 0.3 μ m diamond suspension and a final polish of 0.05 μ m with a colloidal silica suspension.

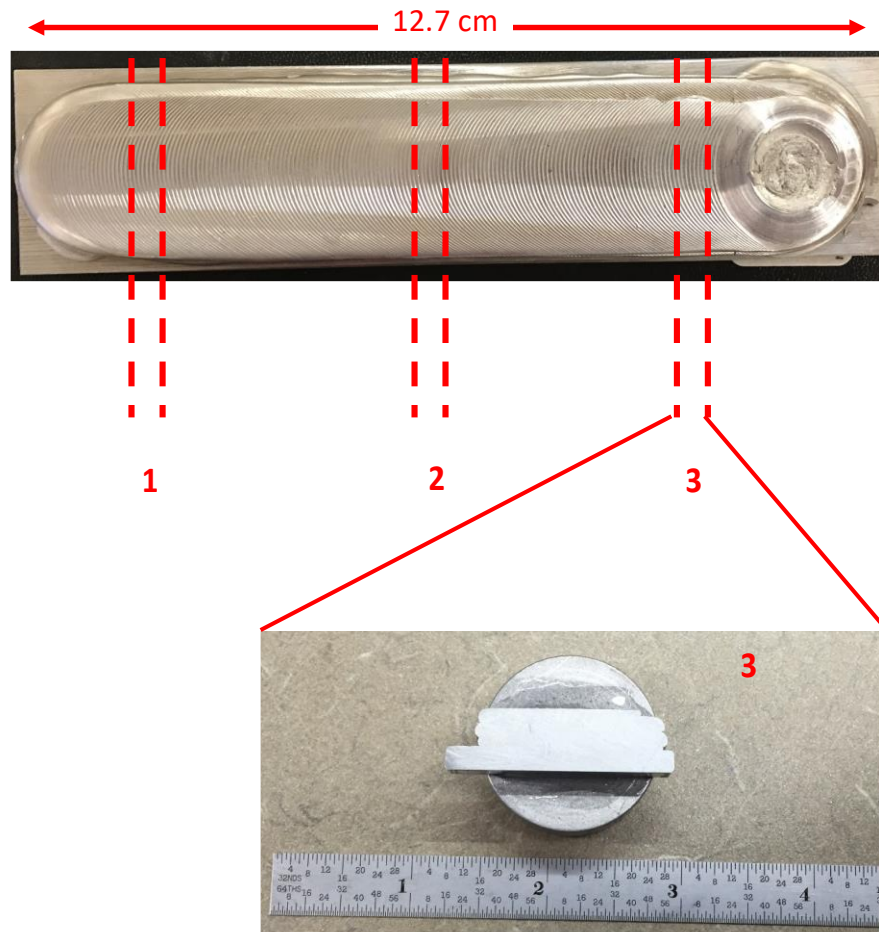


Figure 3-3. Locations of the vickers microhardness testing along the as-build AFS2219.

Vickers microindentation analyzed the hardness through the built cross-section of the as-deposited material in the 3 different locations. A load of 0.1kgf held for 10s was used for the hardness tests, as described in ASTM E384-16 [64]. An indentation grid (Figure 3-11) consisting of 10 rows with spacing between the rows of 1mm and 9 columns spaced at 2.5 mm, which complied with ASTM E384-16 [64] probed the AFS-Deposited cross-section.

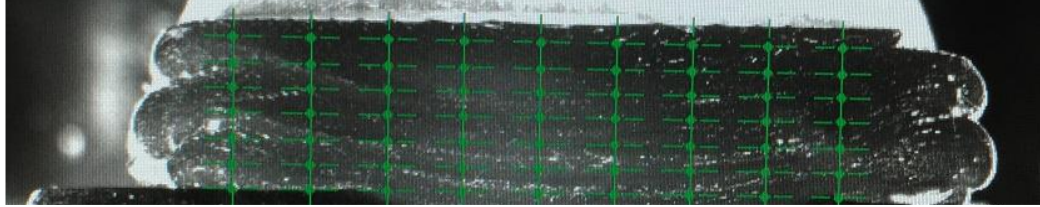


Figure 3-4. Schematic of the microindentation grid used to analyze the transverse cross-section in the three different locations.

A Tescan Lyra FIB-FESEM equipped with an EDAX Hikari Super EBSD camera and an Octane Elite Silicon Drift Detector, was used for EBSD, electron dispersive X-ray spectroscopy (EDX) and fractography. EBSD scans were ran at the same magnification along the build direction over an area of approximately $50 \times 50 \mu\text{m}$, with a step size of $0.1 \mu\text{m}$. The scans were performed at 20 KV and a beam current of 5.5 nA. Line scans were performed from top to bottom of the as-deposited cross-section to spatially quantify grain size. In addition, images were taken in the longitudinal, short transvers and long transverse directions to elucidate the 3D microstructure of the deposition. EBSD data was post-processed using the Neighbor Pattern Averaging and Reindexing (NPAR) option in the EDAX TEAM software, followed by the grain dilation algorithm with setting of a minimum grain size of 2 pixels and a grain must contain multiple rows of pixels. A Transmission Electron Microscope (TEM) FEI TECNAI F-20 was used to study the size, geometry and type of the precipitates. The specimens for the TEM were prepared using the lift-out method with a Focused Ion Beam (FIB) FEI Quanta 200 3D Dual Beam microscope. TEM specimens were lifted out of the filler material (as-received) for comparison purposes and from three locations (top, middle and bottom) in the as build cross-section.

An electromechanical Instron 5185 load-frame with a 50 kN load cell performed the ambient temperature QS tensile and compression experiments at a strain rate of 0.001/s. The HR tensile and compression experiments were conducted on a Kolsky tension/compression bar

located at in The University of Alabama Advanced Materials Diagnostics Laboratory (www.amdl.ua.edu). The 12.7mm diameter 350 Margaging steel striker, incident and transmitted Kolsky bar system performed both the HR tension and compression experiments. The dynamic tensile and compression experiments were performed at a strain rate of 1500/s. Strain was measured using a video camera, were the video strain data was processed using an in-house Matlab routine, that uses a normalized cross-correlation technique (normxcorr2) [52,53]. The same tensile specimen was used for testing of both, QS and HR for comparison purposes of material behavior, especially elongation to failure.

3.3. Results and Discussion

EBSD analysis of the filler material and the as-deposited microstructures provides a comparison of texture and grain size evolving during the deposition process. The EDAX software calculated the grain diameter according to by measuring the area of the grains and assuming a circular grain morphology, and reported an average grain size of approximately 30 μm for the filler material (Figure 3-4A). In the deposited material, the measured average grain size of approximately 2.5 μm shows a significant grain refinement (Figure 3-4B) as compared with the filler material.

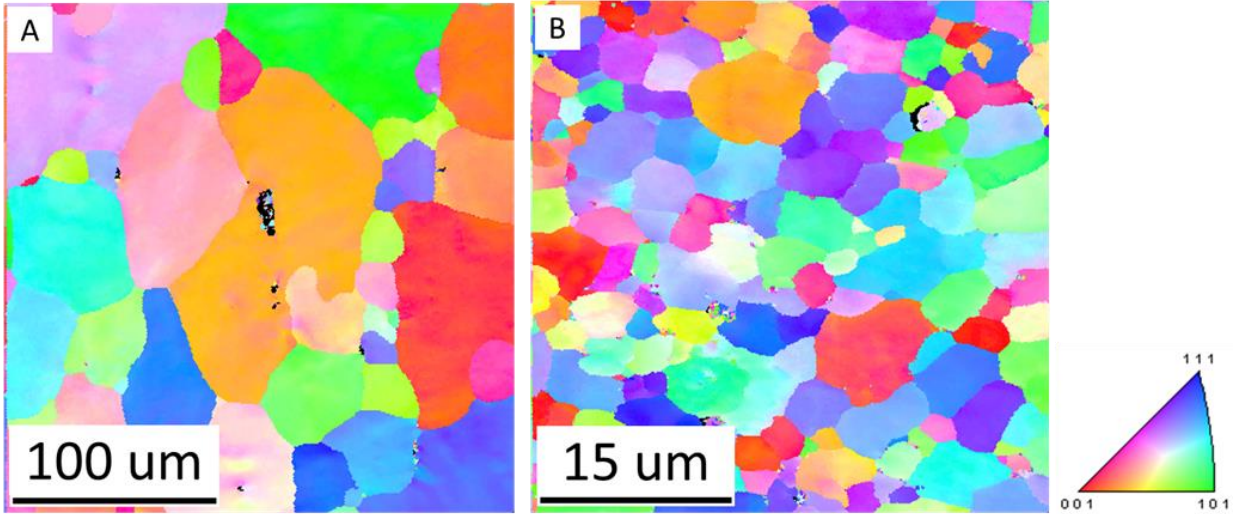


Figure 3-5. Inverse pole figure (IPF) orientation map comparing the microstructure between (A) as-received AA2219-T851 filler material and (B) as-build AFS AA2219. Note the difference in scales between the two maps.

To further elucidate the microstructural changes occurring during the AFS-Deposition process, Figure 3-5 shows a 3D EBSD representation of the filler material and the as-deposited material. In Figure 3-5A, EBSD grain maps correlate that the filler material started as a rolled plate before being machined into a rod for the AFS-Deposition process. In addition, EBSD scans in Figure 3-5B were performed across the as-build cross-section of specimen from the middle of the build to show a 3D reconstruction of the microstructure. Additionally, EBSD was performed from the top to bottom of the as-built cross-section, and the grain size was uniform with no variations between layers.

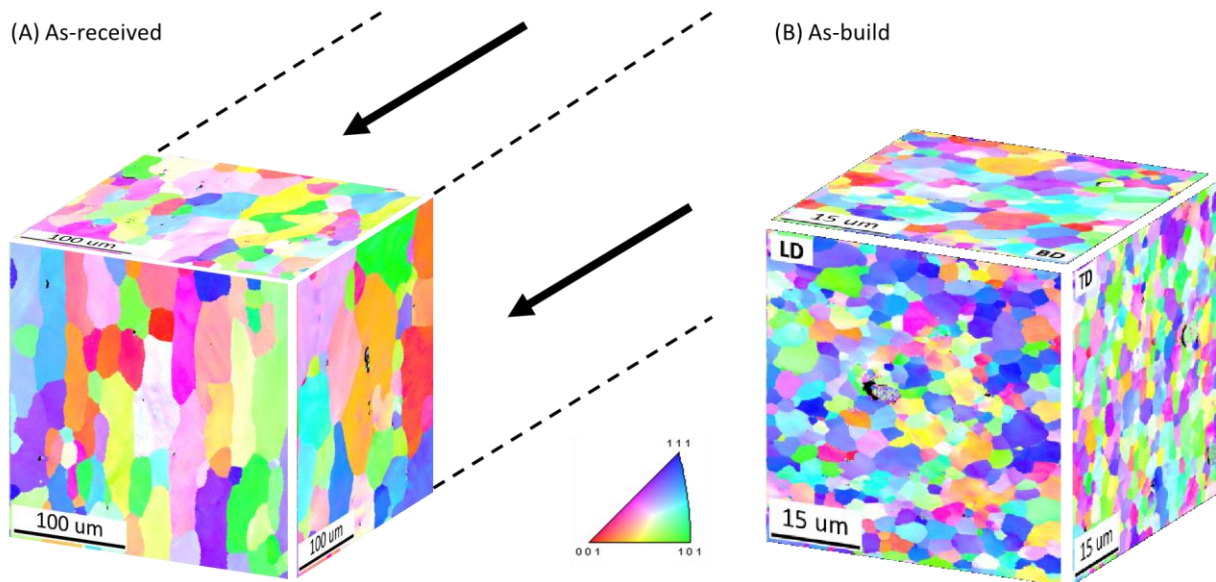


Figure 3-6. 3D IPF orientation map microstructure representation of the (A) as-received AA2219-T851 filler material (100 μm scale bars), compared to the (B) as-built AFS-Deposited AA2219 material (15 μm scale bars). Arrows point to the direction that the material is feed through the tool of the AFS process.

The hardness results from the microindentation experiments are depicted in Figure 3-6 as a bar plot from top to bottom of the AFS-Deposited cross-section. Error bars showing the minimum and maximum hardness values for each respective layer probed have also been included in the plot. The average hardness values plotted in Figure 3-6 reflects a trend of slightly higher hardness values in the top of the material with a gradual decrease towards the bottom of the deposition. However, no statistical difference in hardness from the top to the bottom of the AFS-Deposition is observed [65,66]. Additionally, in Figure 3-6, EBSD IPF maps of the grain morphology and size are shown next to the hardness bars to indicate that the top portion of the deposit (from 0-2 mm) has a grain size of 2.6 μm , the middle region (2-4 mm) has a grain size of 2.5 μm , and the bottom region (4-6 mm) has a grain size of 2.5 μm . Since no difference in the grain size is observed from the top to the bottom of the AFS-Deposition then one can deduce that there is no measurable Hall-Petch effect in the material.

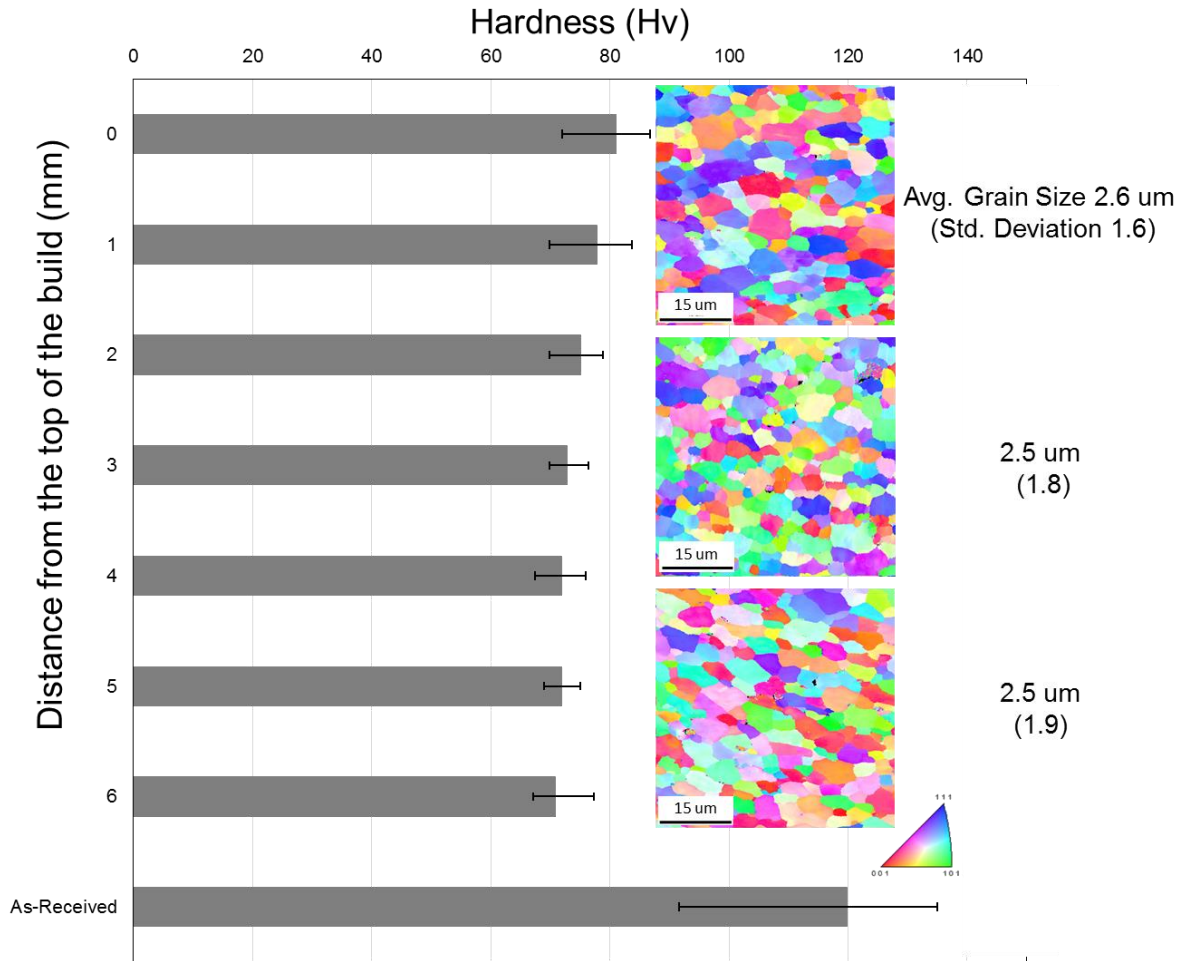


Figure 3-7. Hardness bar chart of the AFS-Deposited AA2219 on the transverse cross-section of the deposited material, with error bars representing minimum and maximum values recorded in that layer. EBSD IPF maps of the top, middle and bottom of the deposition with the corresponding grain size are shown. In the y-axis, 0 is the top and 6 is the bottom of the deposition. There is a total of 6 layers with an average thickness of 1 mm. A load of 0.1kgf held for 10s was used for the hardness tests, as described in ASTM E384-16.

EBSD was also used to probe the microtextures generated in the AFS-Deposition microstructures. The texture plots in Figure 3-7 show the pole figures (PF) of the AFS-Deposition cross section. As seen in Figure 3-7A, the material has a strong texture in the top of the build that weakens toward the middle (Figure 3-7B) and the bottom (Figure 3-7C) of the deposition. Previous research by Montheillet *et al.* [67], showed the four typical torsional textures that may be found in FCC aluminum, and Figure 8 shows the texture fiber type-A in the

{111} PF which can be correlated to the 111 PFs in Figure 3-7. In Figure 3-7A, the $\{\bar{1}11\} < \bar{1}\bar{1}0 >$ fiber component and a split of the $\{1\bar{1}\bar{1}\} < 110 >$ fiber component are evident. Figure 3-9 shows the 111 PFs from the top, middle and bottom at a different angle to elucidate the torsional texture (torsional axis is out of the plane of the page). Research by R.W. Fonda *et al.* [68], reported similar torsional textures for FSW of AA2195.

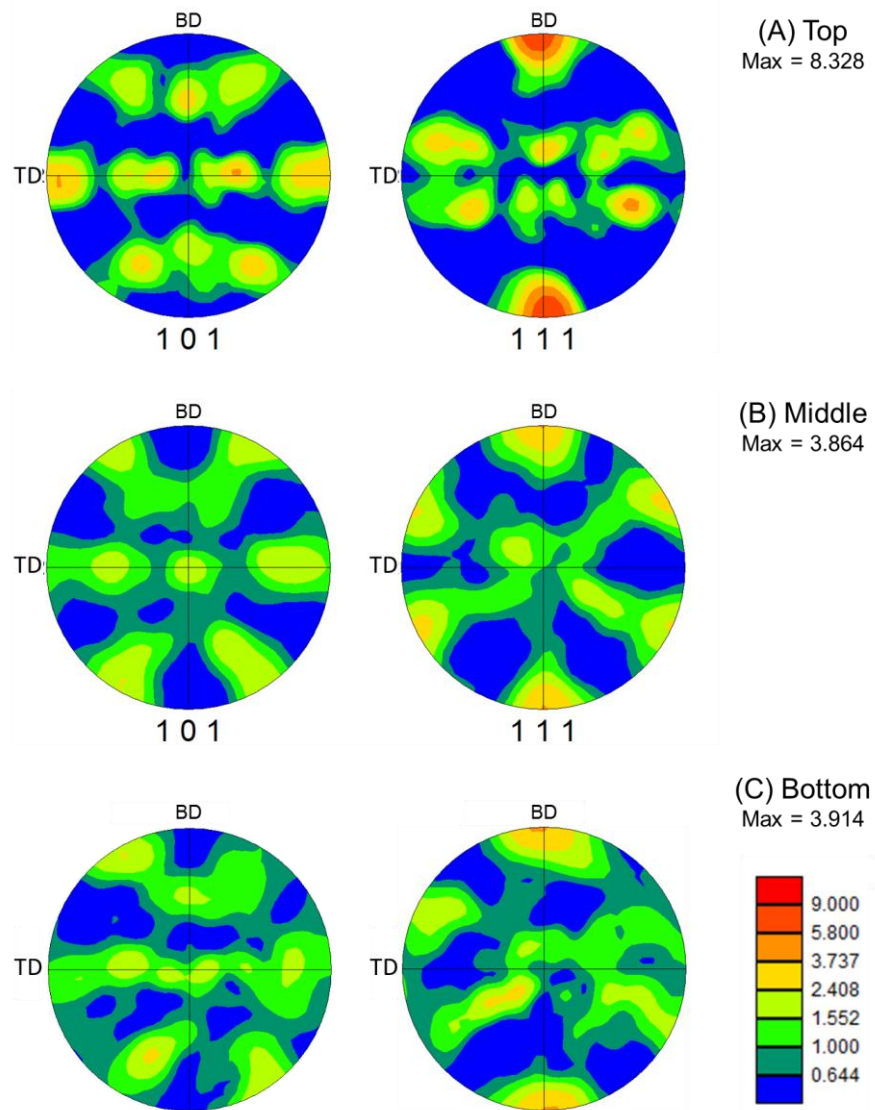


Figure 3-8. EBSD Texture plots of the AFS-Deposited AA2219 build direction (A) representing the texture in the top of the build, (B) the middle, and (C) the bottom.

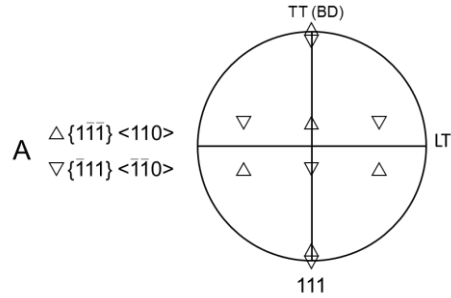


Figure 3-9. Re-drawn image representing one of the four ideal torsional orientations for FCC aluminum as reported by F. Montheillet et al. [67].

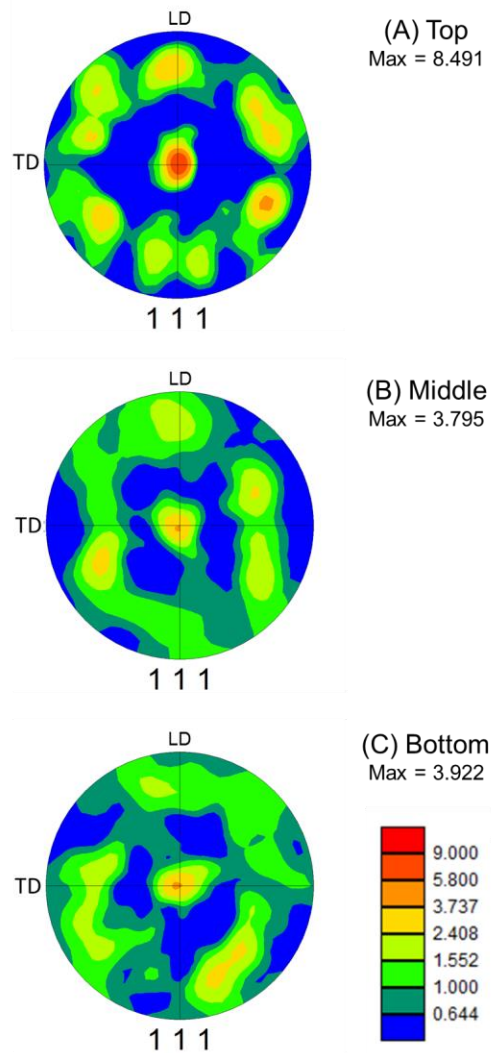


Figure 3-10. EBSD Texture plots of the AFS-Deposited AA2219 build direction (observing from the top) (A) representing the texture in the top of the build, (B) the middle, and (C) the bottom.

TEM analysis further identifies how the material changes from the top to the bottom of the AFS-Deposition. TEM compared the filler rod material to the bottom, middle, and top regions of the AFS-Deposition, which correlates to the EBSD IPF maps shown in Figure 3-6. STEM-HAADF (high angle annular dark field) images from the filler material (Figure 3-10A) show many, small θ' precipitates, as expected from AA2219-T8 and T851 [59]. These precipitates are responsible for the high yield strength levels measured in the as-received material. For the AFS-deposited material, Figures 3-10B, 3-10C, and 3-10D show STEM-HAADF micrographs for the bottom, middle, and top regions, respectively, that contain larger θ (Al_2Cu) precipitates agglomerates [59]. All the STEM micrographs from the bottom, middle and top, depict similar size and type (θ phase) precipitates. No θ' precipitates were observed indicating that there should not be any precipitation strengthening in the AFS-Deposition. It should be noted that it is the spacing between precipitates that is responsible for increased yield strength for large precipitates. The average distance between precipitates in the AFS-deposited material is much larger than in the as-received material, and as such, there is very little precipitation strengthening.

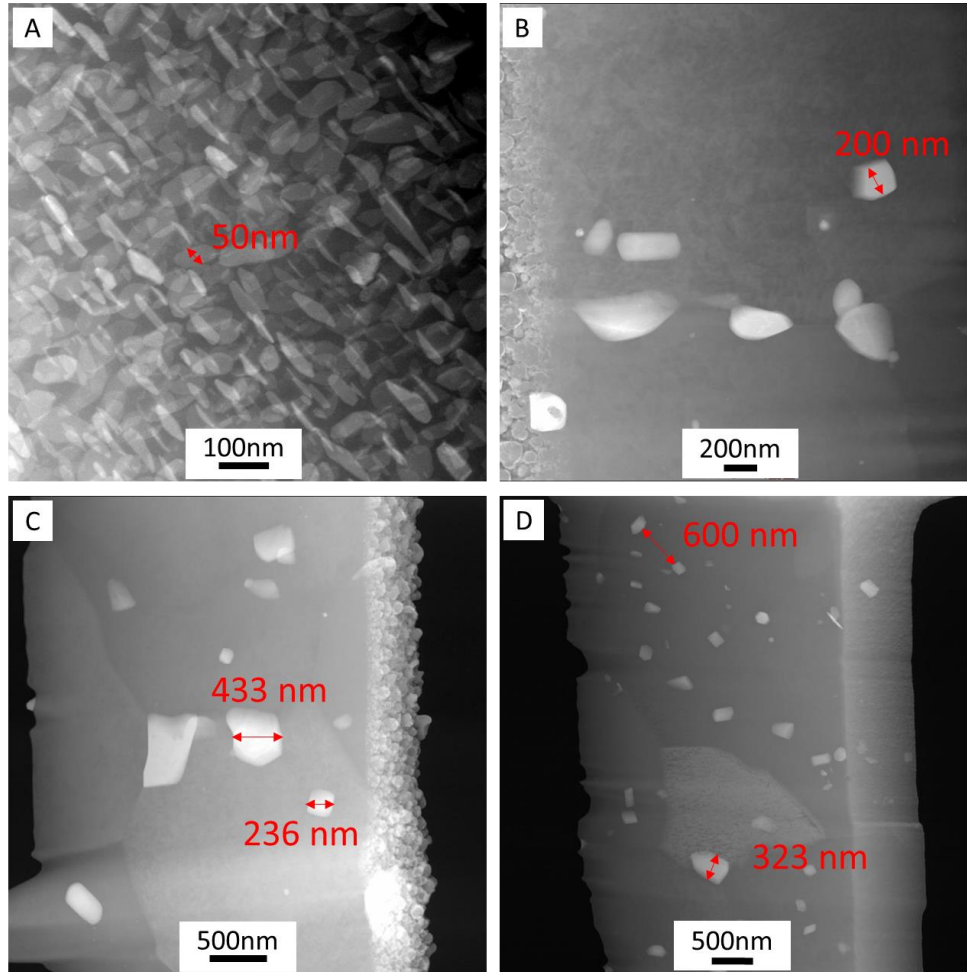


Figure 3-11. TEM micrographs (A) as-received material showing θ' precipitates, (B) bottom, (C) middle, and (D) top, TEM micrographs showing θ precipitates and grain structure from the build cross-section Zone 2 for the AFS-Deposited AA2219 (see Figure 3-6 for reference of locations). (Note: magnification in Figure 3-10 (A) is much higher than B-D)

Next, tension and compression QS and HR experiments examined the stress-state and strain rate dependence of the AFS-deposited material. Figure 3-11 plots the average (3 specimens) QS and HR compressive behavior up to a strain of 0.25 for the TD, DB, and LD directions with uncertainty bands corresponding to minimum and maximum, experimental values. The QS compressive data shows a near isotropic response of the AFS-Deposition, with an average YS of approximately 145 MPa for the TD, 140 MPa for the BD, and 150 MPa for the LD directions. For the HR compressive material behavior, the TD has a higher yield than the BD

and LD directions, with an average YS of approximately 295 MPa for the TD, 238 MPa for the BD, and 225 MPa for the LD directions. In QS, the material experiences more strain hardening and higher UTS than at HR. However, as expected the HR achieves higher YS than QS, but the HR does not experience as much strain hardening and eventually plateaus. The QS and HR compression experiments were stopped at a maximum strain of 0.25 mm/mm since the material did not fracture.

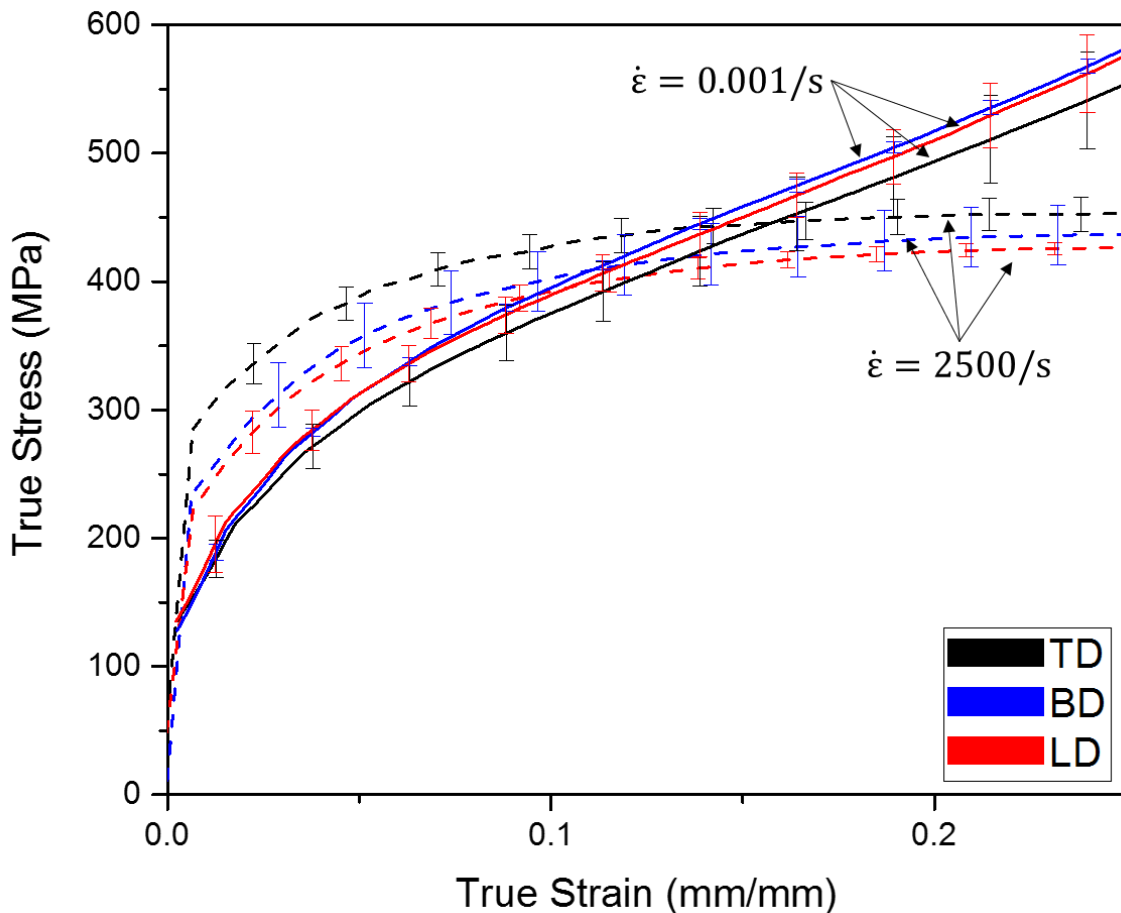


Figure 3-11. Compression testing results comparing the long transverse, short transverse, and longitudinal directions in quasi-static (0.001/s) and high rate (2500/s). The quasi-static long transverse, short transverse and longitudinal achieved a YS of 145, 140, and 150 MPa, respectively. The high rate long transverse, short transverse, and longitudinal achieved a YS of 295, 238, and 225 MPa, respectively. All compression tests were stopped at a strain of 0.25.

The average QS and HR tensile behavior for the TD and LD directions with the associated uncertainty bands corresponding to the maximum and minimum experimental values can be seen in Figure 3-12. The QS tensile TD specimens achieved an average YS of 148 MPa, an UTS of 363 MPa, and ϵ_f of 0.24 mm/mm. The QS tensile LD specimens achieved an average YS of 143 MPa, an UTS of 355 MPa, and ϵ_f of 0.26 mm/mm. The QS tensile specimens in both directions exhibited a ductile failure (Figure 3-13) with strain hardening and softening after yielding. Similar to the compressive behavior, the material shows more strain hardening in the QS case, when compared to the HR, which after yielding exhibits a stress-strain curve plateau. The HR tensile TD and LD specimens achieved average YS of 235 and 240 MPa, UTS of 240 and 240 MPa, and ϵ_f of 0.37 and 0.37, respectively. The HR fractography (Figure 3-14) revealed a ductile behavior with a cup-cone fracture surface. For both QS and HR cases, isotropic behavior in the two orientations are observed for the tensile mechanical behavior.

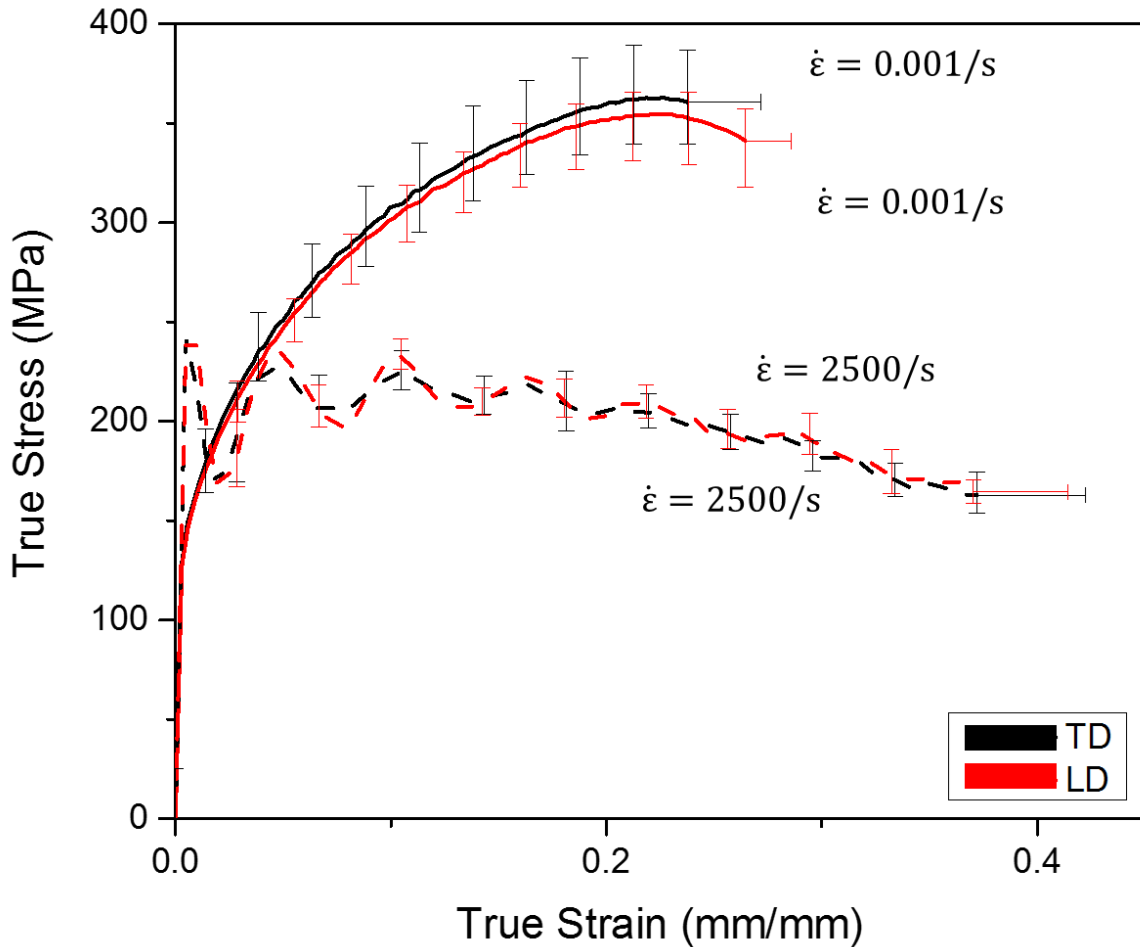


Figure 3-12. Tensile results comparing the long transverse and longitudinal directions in quasi-static (0.001/s) and high rate (2500/s). The quasi-static long transverse and longitudinal achieved a YS of 148 and 143 MPa, UTS of 363 and 355 MPa and ϵ_f of 0.24 and 0.26, respectively. The high rate long transverse and longitudinal achieved a YS of 235 and 240 MPa, UTS of 240 and 240 MPa and ϵ_f of 0.37 and 0.37, respectively.

SEM fractographic analysis of both QS and HR (Figure 3-10 and 3-11, respectively), show ductile failure behavior for the AFS-Deposition AA2219 material. SEM QS fractography images with increasing magnifications are shown in Figure 3-13A, 3-13B, 3-13C, and 3-13D. Similarly, the HR SEM fractography images are shown in increasing magnifications in Figure 3-14A, 3-14B, 3-14C, and 3-14D. Both QS and HR fracture surfaces exhibited microvoids and dimples.

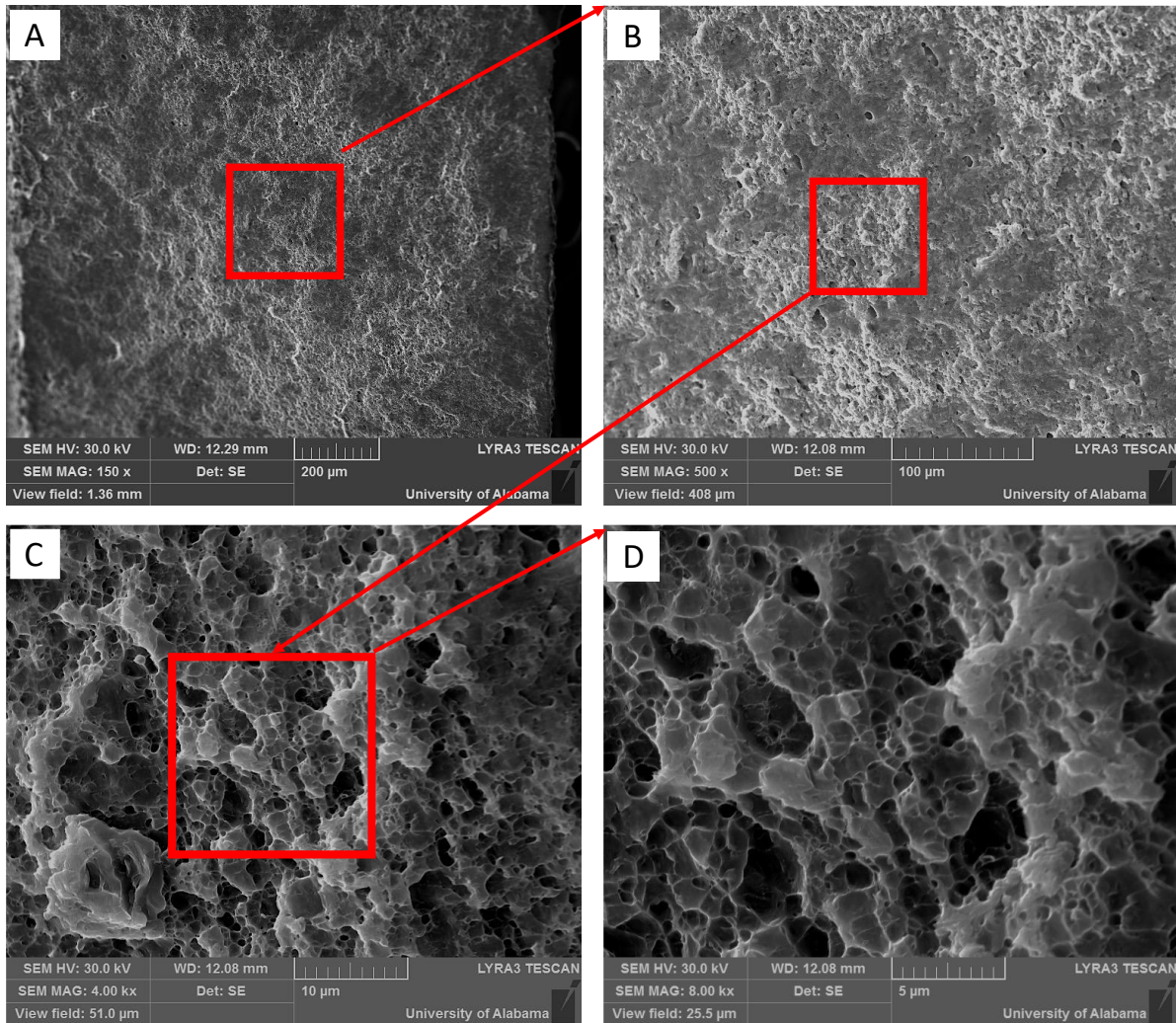


Figure 3-13. Fractography of QS (strain rate of 0.001/s) tensile specimens tested to failure. 3-10A, 3-10B, 3-10C and 3-10D (scale bars are 200, 100, 10, and 5 micron, respectively) are SEM images.

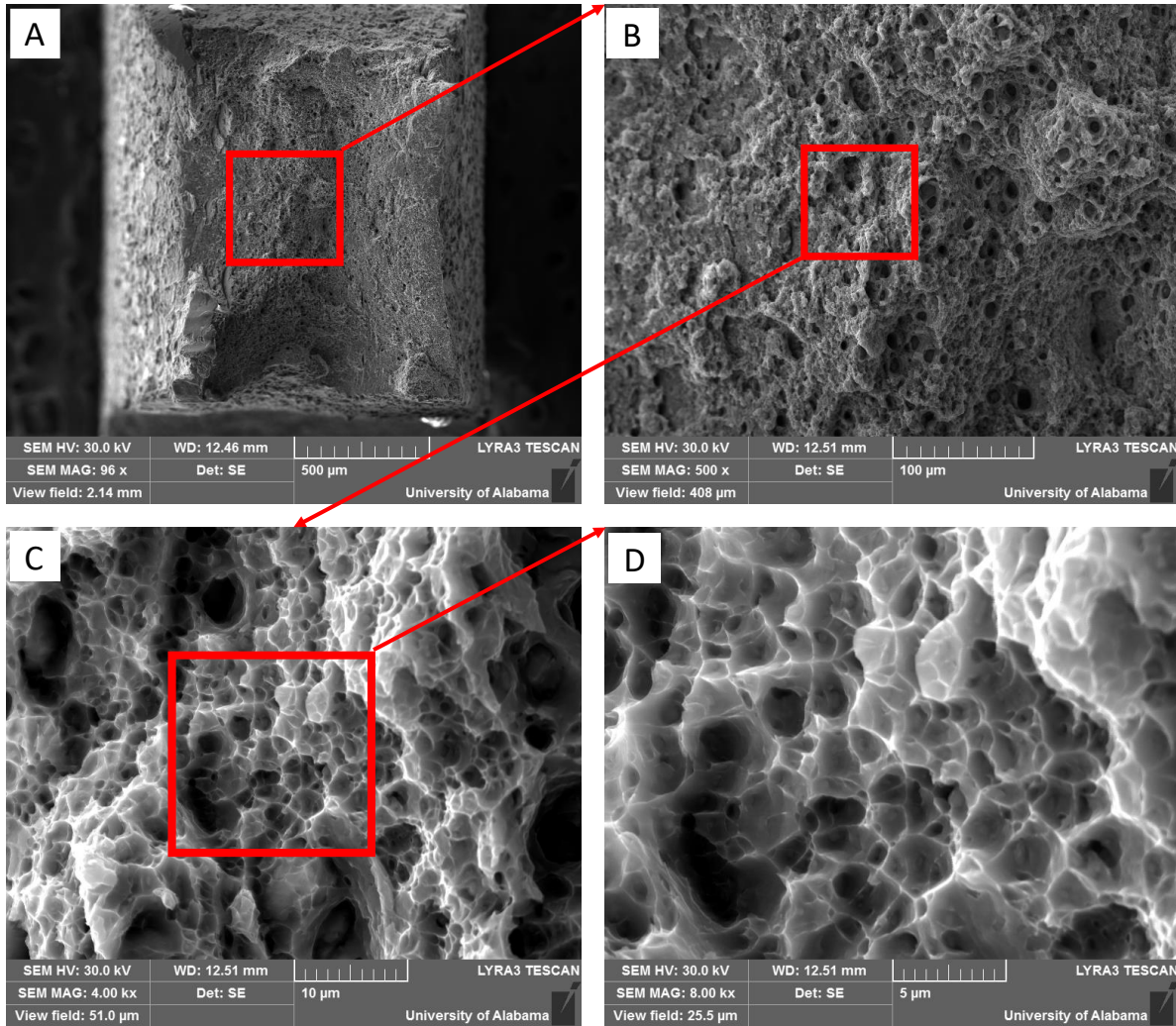


Figure 3-14. Fractography of HR (strain rate of 2500/s) tensile specimens tested to failure. 3-11A, 3-11B, 3-11C and 3-11D (scale bars are 500, 100, 10, and 5 micron, respectively) are SEM images.

The averaged AA2219 AFS-Deposition tensile properties are compared to AA2219 tensile properties from various manufacturing or joining techniques are provided in Table 3-2. The AFS-Deposition process (highlighted in gray in Table 3-2) resulted in higher YS, UTS and ϵ_f than AA2219-O and as-deposited EBF AA2219. Additionally, AA2219 AFS-Deposition resulted in better mechanical properties than FSW 2219-O. The AFS-Deposition AA2219 mechanical properties are below those of AA2219-T851, but as shown previously in the Figure 3-10 TEM data, the nano-precipitates that provide the precipitation strengthening of AA2219

were eliminated during the AFS-Deposition. Previous research on EBF by Taminger and Hafley [29], showed that after depositing the AA2219 and performing the T62 heat treatment resulted in material properties of AA2219-T62 suggesting AFS-Deposition AA2219 would be heat treatable as with the EBF AA2219. The strain to failure was not directly compared to published literature data since this study used a subscale specimen for both QS and HR experiments instead of a larger ASTM E8 tensile coupon, but a column of strain to failure is provided for reference in Table 3-2.

Table 3-2. Comparison of AA2219 YS, UTS, and ϵ_f of different manufacturing processes.

Condition	YS (MPa)	UTS (MPa)	ϵ_f (%)
AA 2219-O [61]	75	170	18
AA 2219-T62 [61]	290	415	10
AA 2219-T851 [61]	350	455	10
AFS-Deposited AA 2219 (As Deposited) [This research]	143-148	355-363	24-26
FSW AA 2219-T8 (WNZ) [60]	208-210	363-366	18.6-21.3
FSW AA 2219-T6 [11]	-	255-336	-
FSW AA 2219-O [8]	86.6-111.4	150.6-187.8	4.9-10.2
EBF AA 2219 (As Deposited) [29]	112	283	19.4
EBF AA 2219 (Deposit+T62) [29]	290	416	11.1

3.4. Conclusions

This is the first manuscript to detail the microstructure and mechanical properties of AFS-Deposited AA2219 fabricated from AA2219-T851 filler rod material. EBSD results revealed a refined, equiaxed microstructure which is likely formed due to DRX [16–18]. A uniform grain size was found from the top to the bottom of the AFS-Deposition cross-section. The material hardness had a small variation from top to bottom, but taking into consideration the maximum and minimum from that location, from a statistic point of view, the hardness was the same. EBSD PFs showed that the material has a strong torsional fiber A texture in the top of the

build, and this texture gets weaker in the middle and bottom sections. TEM showed that there are no θ' precipitates in the as-deposited cross-section, therefore no precipitation strengthening should be expected. The mechanical properties of the as-build AFS-Deposition AA2219 material are better than AA2219-O, but the values are below those of AA2219-T851 since there are no θ' precipitates providing strength to the material. As mentioned above, previous research by Taminger and Hafley [29] showed that after applying the T62 temper to the as-build EBF material, the materials mechanical properties matched those of a AA2219-T62. This is extremely important, since being able to regain those microstructural and mechanical properties that the T62 and T851 tempers provide is crucial for the applications of this alloy. The strain rate dependence was examined, and at HR the material experienced higher yield strength and lower ultimate strength. At HR, the material strain hardening was less than when tested at QS, it can be seen that the material stress-strain curve plateau after yielding. In addition, the tensile specimens in HR specimens also exhibited more ϵ_f than in the tensile specimens in QS. The strain to failure was not compared to data found in the literature since the specimen used in this research was a subcale size specimen. Further research must be done exploring the material mechanical properties and microstructure with different tempers on the as-build material, as well as its fatigue properties.

CHAPTER 4
PLASTICITY AND DAMAGE MODELING OF THE BAUSCHINGER EFFECT IN
ADDITIVE MANUFACTURED AFS-DEPOSITION AA2219

4.1. Introduction

This research will be the first application of a physics-based microstructure-dependent internal state variable (ISV) plasticity and damage material model to capture the mechanical response of an additively manufactured aluminum alloy (AA) 2219 via the additive friction stir deposition (AFS-Deposition) process. As described in previously in Chapter 2 and 3, during the AFS-Deposition process, solid or powder metals are pushed through a non-consumable rotating cylindrical tool. Herein, added layers are deposited and metallurgically bonded to substrate material or previously deposited layers by the heat generated from the rotating tool through plastic deformation of the filler material. Once a layer has been added, the tool height increases, and starts the deposition of the next layer. The AFS process results in beneficial properties such as grain refinement, homogenization and reduced porosity (fully dense). This process will experience temperatures similar to those in the weld nugget zone (WNZ) in friction stir welding (FSW), ranging from 0.6-0.9 T_m , with T_m being the melting point of the material [45]. AFS-Deposition is highly scalable with AA deposition rates reaching over 1000 cm^3/hr , which allows for AFS-Deposition being used for repairs, coatings, and building components.

A motivating factor driving the research for physics-based history dependent material modeling of AFS-Deposition components is the ability to accurately capture the stress-state and strain rate dependence in the material caused by variations in material microstructure from the

AFS-Deposition processing of new or repaired components. The modeling approach proposed here has been previously implemented to use the microstructural features of wrought, cast, and powder metal materials to capture stress-state, strain-rate, and temperature dependence [50,62,63,69–76]. Finite element (FE) methods coupled with internal state variables (ISV) are used to model the plasticity and damage state at the structural scale. The physically-based model including microstructure-based ISVs for plasticity and damage was originally presented by Bammann and Aifantis [77] and Bammann et al. [78] and later modified to account for nucleation, growth, and coalescence of voids by Horstemeyer and Gohkale [69], Jordon et al. [75], and Allison et al. [62]. The ISV model incorporates microstructural content and is consistent with continuum level kinematics, kinetics, and thermodynamics. These features allow the ISV model to capture large deformations at the structural scale using the kinematic and isotropic hardening, while microscale damage is obtained from the microstructural features. The benefits of the ISV model arise from the inclusion of structure-property relationships identified from microstructural characterization and experimentation.

The Bauschinger effect (BE) is an important concept, vital in the accurate prediction of cyclic stress-strain response of ductile materials such as metals. The BE can be described as a reduction in the flow stress during the reversing portion of an initial applied loading [79]. In the case of polycrystalline metals such as steels and aluminums, the BE is strongly related to the progression of internal stresses as a result of both static and dynamic strain histories [80]. Previous research has shown that the BE and its degree in polycrystalline metals is dependent of the grain alignment and variations in flow-stress between grain boundaries, intergranular regions and second phase particles [81–83]. The ISV plasticity-damage model capture the BE through the use of the kinematic and isotropic hardening, softening components and damage [84]. The

ISV model has been successfully used to capture the behavior and damage, and the BE of different aluminum alloys and steels [50,63,75,85–87].

As mentioned before, the ISV model uses kinematic and isotropic hardening to help capture deformations of the material at the macro scale. To understand this hardening relationship, calculating the kinematic and isotropic hardening relationship in the material is warranted for a high fidelity model.

Research by Jordon et al. [85,88] introduced a parameter called the ratio of kinematic hardening to isotropic hardening (RKI) explained in Equation 1 to determine the appropriate relationship. This parameter uses the concept of yield surface for both the kinematic and isotropic hardening relation to help quantify the Bauschinger effect.

$$RKI = \frac{(\sigma_f + \sigma_r)}{(\sigma_f - \sigma_r) - (2 * \sigma_y)} \quad (1)$$

Where σ_f represents the forward stress, σ_r represents the reverse yield and σ_y is the yield strength at initial yield.

Another parameter used to capture the commonly seen decrease in reverse yield in the BE in polycrystalline materials is the Bauschinger Stress Parameter (BSP) shown in Equation 2 [89]. The BSP, which has been applied to various aluminum alloys [90,91], is the ratio between the development of the forward and reverse stress (Equation 2).

$$BSP = \frac{|\sigma_f| - |\sigma_r|}{|\sigma_f|} \quad (2)$$

While both parameters, BSP and RKI, can be used quantify the BE, the BSP does not

appropriately quantify the degree of kinematic and isotropic hardening, which the RKI does.

This manuscript, a first of its kind for AFS AA2219, includes correlating the ISV model to the monotonic experimental results that capture the isotropic and kinematic plasticity mechanical response. The pertinent equations and explanation of the equations are provided in Appendix A.

4.2. Model Set-up and Calibration on AFS-Deposition AA2219

To calibrate the plasticity-damage model, a single set of constants were determined to capture the different stress states the AFS-Deposition AA2219. One set of the constants was determined from experimental true stress-strain curves for the tension and compression data. Additionally, microstructural information and data from the open literature were used as the other model constants.

4.2.1. Additive Manufactured AFS-Deposition Material

Aeroprobe Corporation, creator and patent holder for the AFS-Deposition process, fabricated and provided the AFS-Deposition AA2219 material by pushing a solid filler rod of AA2219-T861 material through a hollow rotating tool onto an AA2219 T851 plate substrate. As depicted in Figure 4-1, the AFS-Deposition process deposits layer by layer when filler material gets stirred together with a combination of heat generated by friction between the filler material and the tool shoulder under hydrostatic pressure, which plastically deforms the material. A more detailed explanation of AA2219 AFS-Deposition may be found in Chapter 3. Table 4-1 lists the average chemical composition of this alloy.

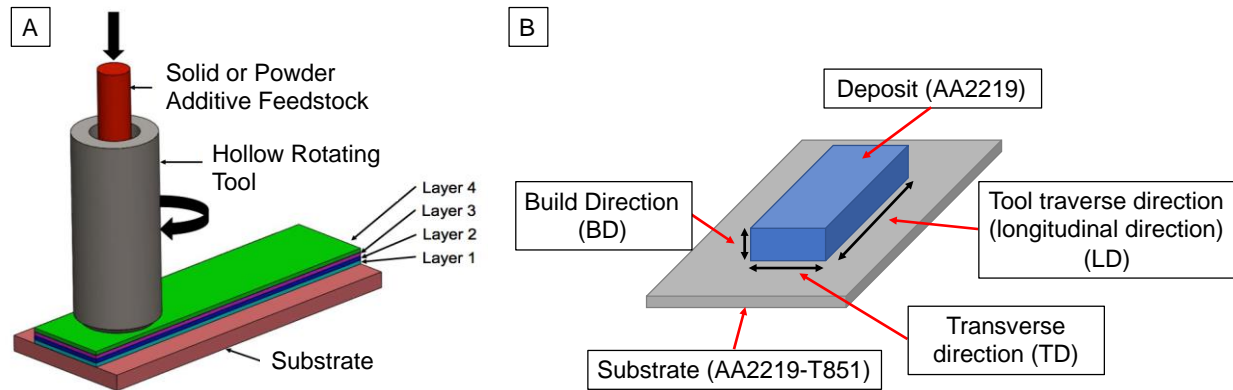


Figure 4-1. (A) AFS process with the extrusion of the solid material through the hollow rotating tool layer by layer. (B) Schematic of the AFS deposition of AA2219 identifying the three directions (LD, BD, and TD).

Table 4-1. Chemical composition of AA2219 [61].

Elements	Al	Cu	Mn	Ti	V	Zr
Percentage	93.0	6.3	0.30	0.06	0.10	0.18
	6					

4.2.2 Experimental Procedure

A series of experiments at various stress-states and strain rates were performed to quantify the structure-property relations needed for calibrating the ISV plasticity-damage model. An Instron 5185 load-frame with a 50 KN load cell performed the ambient temperature QS tensile and compressive experiments. A subcompact flat, dog-bone shaped specimen with a 4.5 mm gauge length, 2.0 mm width and 1.5 mm thickness was used for tensile testing while strain was recorded with a video camera and with an in-house Matlab routine, the video strain data was calculated using a normalized cross-correlation technique (normxcorr2) [52,53]. Cylinders with a 6mm diameter and 6 mm length were used for the compressive testing. A complete explanation of the structure-property experiments performed may be found in Chapter 3.

To calculate the BSP and the RKI for calibrating the model, BE experiments were performed in tension followed by compression to 1%, 3% and 5% strain and compression

followed by tension to 1% and 3% strain. For these experiments, and EDM machined flat, dog-bone shaped specimens with 12 mm gauge length, 3.17 mm thickness and 3.17 mm width. The BE experiments were performed in an MTS Landmark servohydraulic load-frame equipped with a 25 KN load cell. All data acquisition was performed by an MTS Flex Test 40 controller and strain was controlled using an E97356 Epsilon extensometer.

To obtain the microstructural constants, the 3D microstructure was quantified in the longitudinal direction (LD), build direction (BD) and transverse direction (TD) of the as-deposited material. A wire EDM machined specimens in all the orientations in the beginning, middle and end of the deposition and at bottom, middle, and top locations of these spatial regions as depicted in Figure 4-2 and discussed in Chapter 3. By obtaining all these regions and orientations for microstructural analysis, a statistically significant representation of the as-deposited microstructure was determined to identify any spatial dependence in the as-deposited material. For the microstructural characterization, specimens were first ground down to 1200 grit paper, then final polished down to 0.05 μm colloidal silica. Imaging and Electron Backscatter Diffraction (EBSD) used a Tescan Lyra FIB-FESEM equipped with a EDAX Hikari Super EBSD camera and an Octane Elite Silicon Drift Detector to determine average grain size. All the EBSD scans were done at the same magnification using a 50 x 50 μm area with a step size of 0.1 μm . Backscatter secondary images were taken to quantify the particle distribution and size. Additionally, for particle analysis, ImageJ software was used to calculate the particle size, area fraction and nearest neighbor distance. The same Tescan Lyra FIB-FESEM obtained the damage parameters from fracture surface image analysis on a minimum of four SEM images for three specimens.

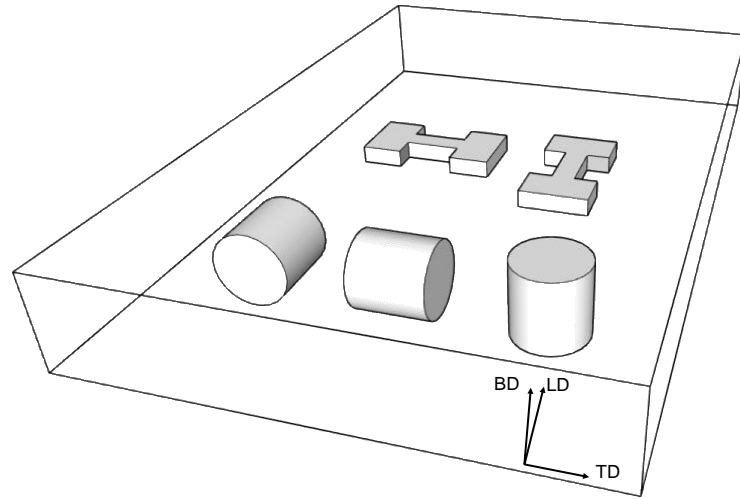


Figure 4-2. Schematic of specimen orientation in the build material.

4.3. Results and Discussion

The EBSD scans reported in Chapter 3, exhibited a uniform grain size from top to bottom of the as-deposited material, with an average grain size of approximately $2.5\ \mu\text{m}$. Figure 4-3 is a 3D reconstruction of the microstructure, and shows the equiaxed grain structure observed in all three orientations (LD, BD, and TD). Furthermore, the SEM backscatter images (Figure 4-4) quantified the area fraction and size of the θ phase particles in the as-deposited material. For each orientation, five areas were scanned to attain an average value. Table 4-2 shows the determined values with a particle size diameter of $2.7\ \mu\text{m}$, particle area fraction 0.037, a particle nearest neighbor distance of $7.9\ \mu\text{m}$ and the average grain size of $2.5\ \mu\text{m}$.

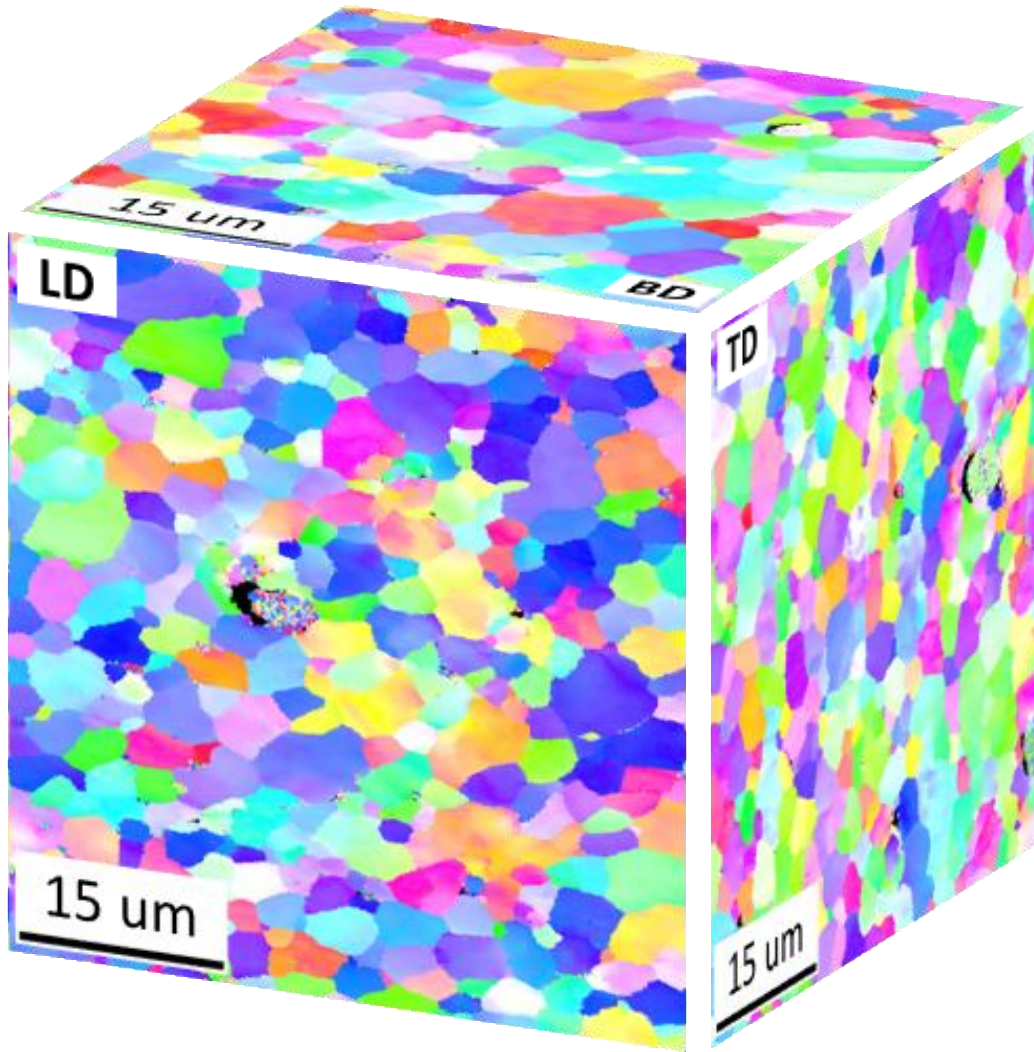


Figure 4-3. EBSD IPF maps showing the grain microstructure in the L, TT, and LT directions.

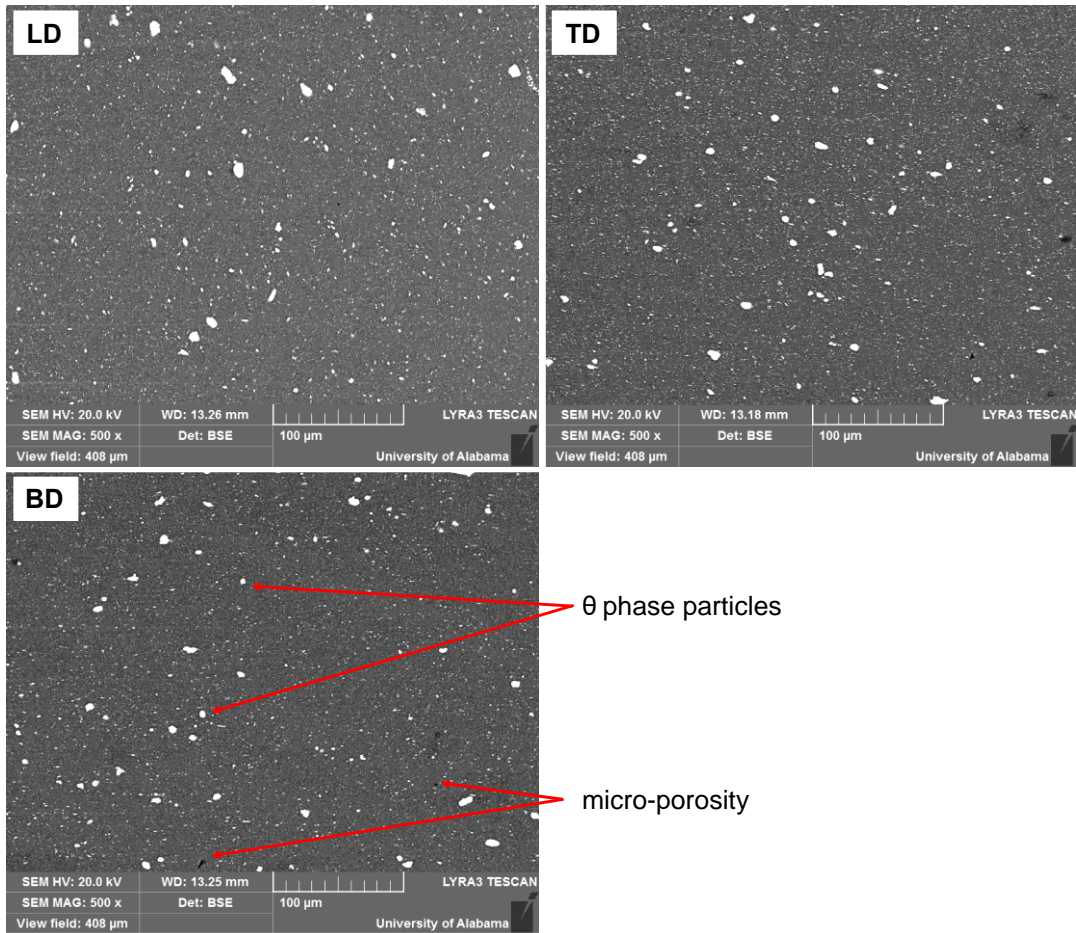


Figure 4-4. SEM backscattered images of the θ phase in the LD, TD, and BD directions.

Table 4-2. Average values of particle size diameter, particle area fraction, particle nearest neighbor distance and grain size. Data was obtained from the middle of the build in the three directions and averaged.

Feature	Particle size (μm)	Particle area fraction	Particle NND (μm)	Grain size (μm)
Average value	2.7	0.037	7.9	2.5

To determine the plasticity-damage constants, a DMGFIT software developed by Mississippi State University (MSU) based on the ISV plasticity-damage model [92] was used. Constants for tension, compression, tension–followed-by-compression and compression–followed-by-tension were all determined at once (Figures 4-5 and 4-6). Since the algorithm tried

to optimize the entire dataset (all the curves) at once, all the curves were not captured exactly by the model. Nonetheless, the model was able to successfully capture material behavior within the uncertainty bands, as seen in Figure 4-5. Figure 4-5 shows the QS tensile and compressive stress-strain plot, where the error bars delimit the experimental maximum and minimum values, the dashed (compression) and dotted (tension) lines are the experimental averages, and the solid line is the model fit for each stress state.

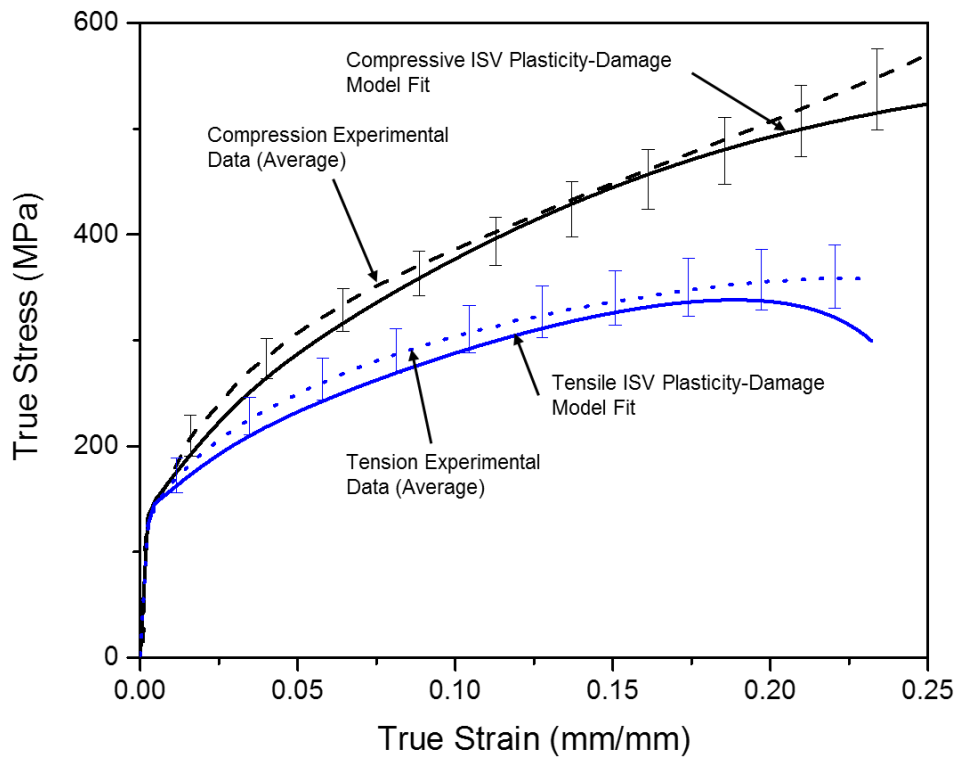


Figure 4-5. Internal state variable plasticity damage model calibration for compression (black) and tension (blue) in QS (0.001/s).

Figure 4-6 shows BE stress-strain plots, where the dashed line represents experimental data and the solid line represents modeled data. As stated before, since the software algorithm is fitting a whole dataset, not only one curve with one set of constants, there may be possible

variations between the experimental and model data. Table 4-3 shows the yield stress, reverse yield stress, forward stress, kinematic hardening, isotropic hardening, the BSP and RKI values for the different test performed. Yield stresses were calculated using the 0.2% strain offset definition. It is observed from the RKI column in Table 4-3 and from Figure 4-7 that the value increases almost linearly with an increase in applied strain. The same can be observed for the BSP value from Table 4-3. The RKI value increase with an increase in prestrain is an indication that the growth of kinematic hardening is greater than the isotropic hardening. This, in turn, suggests that anisotropic hardening grows more than isotropic hardening. Similar trend on the RKI value was observed by Jordon et al. [85] in AA7075-T651.

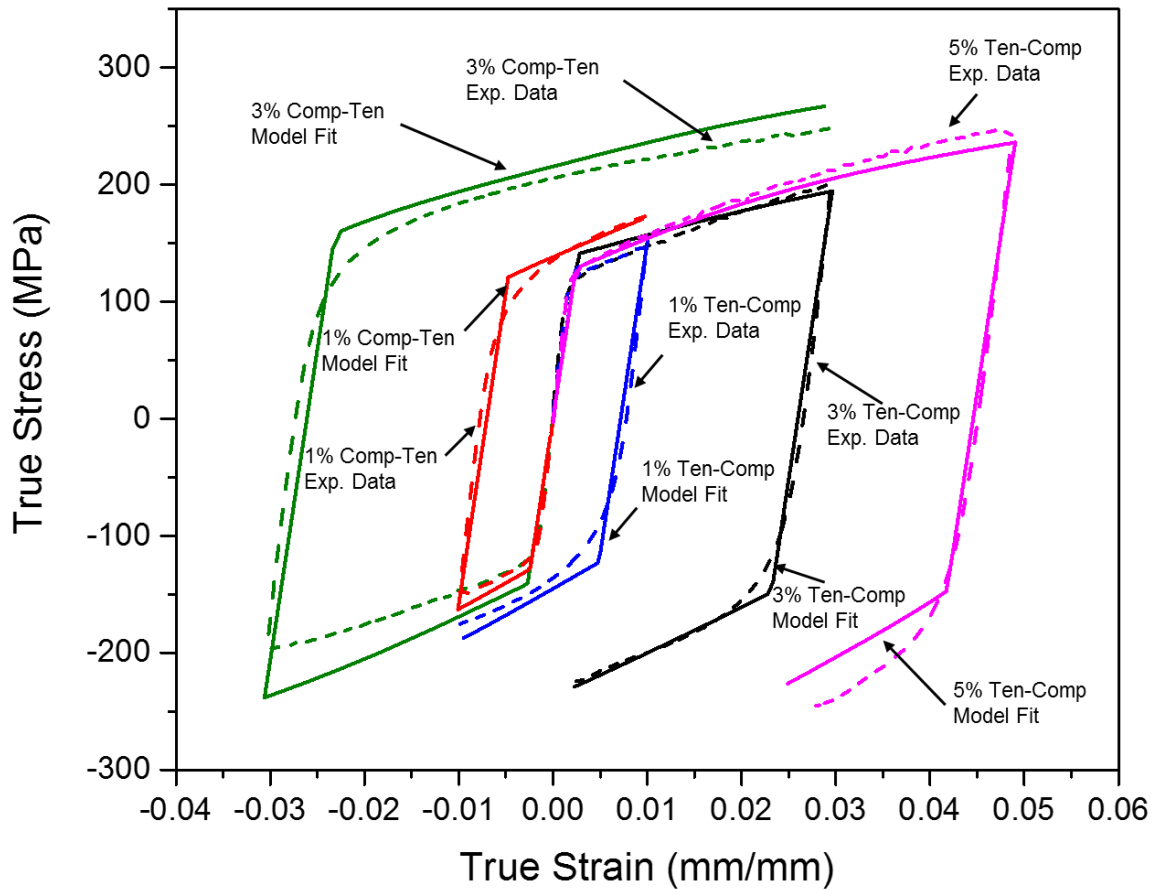


Figure 4-6. A comparison of the internal state variable plasticity-damage model and experimental data illustrating the Bauschinger effect for AFS AA2219 under different directions (tension followed by compression and vice versa) and different prestrain levels (1% and 3%).

Table 4-3. Bauschinger effect results for different prestrains and directions for AFS AA2219.

Prestrain	Direction	σ_y (MPa)	σ_r (MPa)	σ_f (MPa)	a	R	BSP	RKI
1%	Ten-Comp	125	98	147.1	122.6	100.5	0.334	1.220
3%	Ten-Comp	125	130	201.4	165.7	89.3	0.355	1.856
5%	Ten-Comp	129	157	247.9	202.45	83.6	0.367	2.423
1%	Comp-Ten	127	106	152	129.0	104.0	0.303	1.240
3%	Comp-Ten	127	118	197.5	157.8	87.3	0.403	1.808

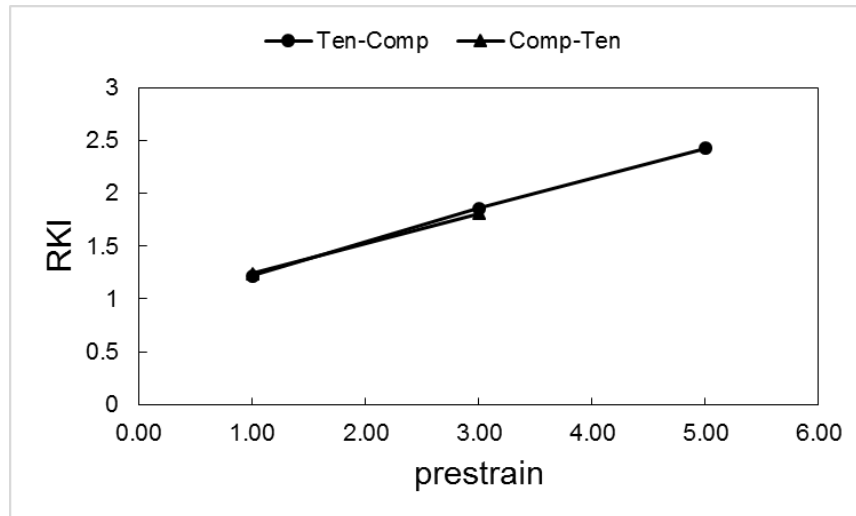


Figure 4-7. Experimental values of the ratio of kinematic to isotropic hardening (RKI) plotted against the maximum forward prestrain.

As mentioned previously, for the damage parameter information, fractography analysis was performed on the fractured tensile specimens to measure the final void density of the material. Four SEM images from three different specimens provided the average final void density per millimeter squared ($\#/mm^2$). Figure 4-8A shows a low magnification SEM image of the fracture surface, and Figure 4-8B shows an example of a magnified SEM image used for the analysis.

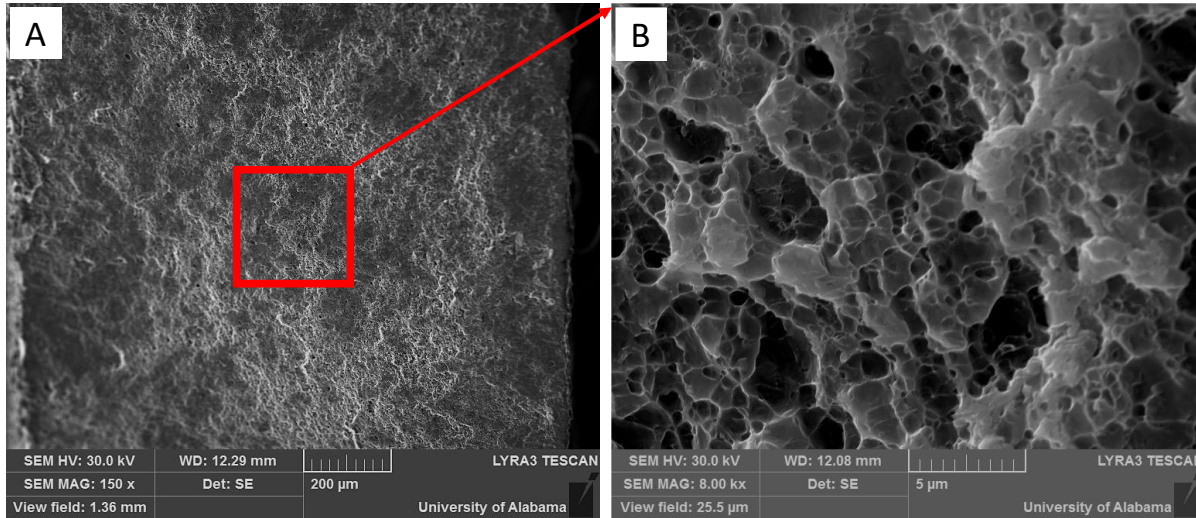


Figure 4-8. SEM images of the fracture specimen for the QS (strain rate of 0.001/s). (A) At a magnification of 150x. (B) At a magnification of 8000x.

Next, the DMGFIT software performed a simulation of the damage parameters to verify how well the model could capture the final void density (nucleation) on the material. Figure 4-9 presents a plot of the simulated void density results compared against the measured value of the void density measured from the fracture surfaces (error bars represent minimum and maximum calculated).

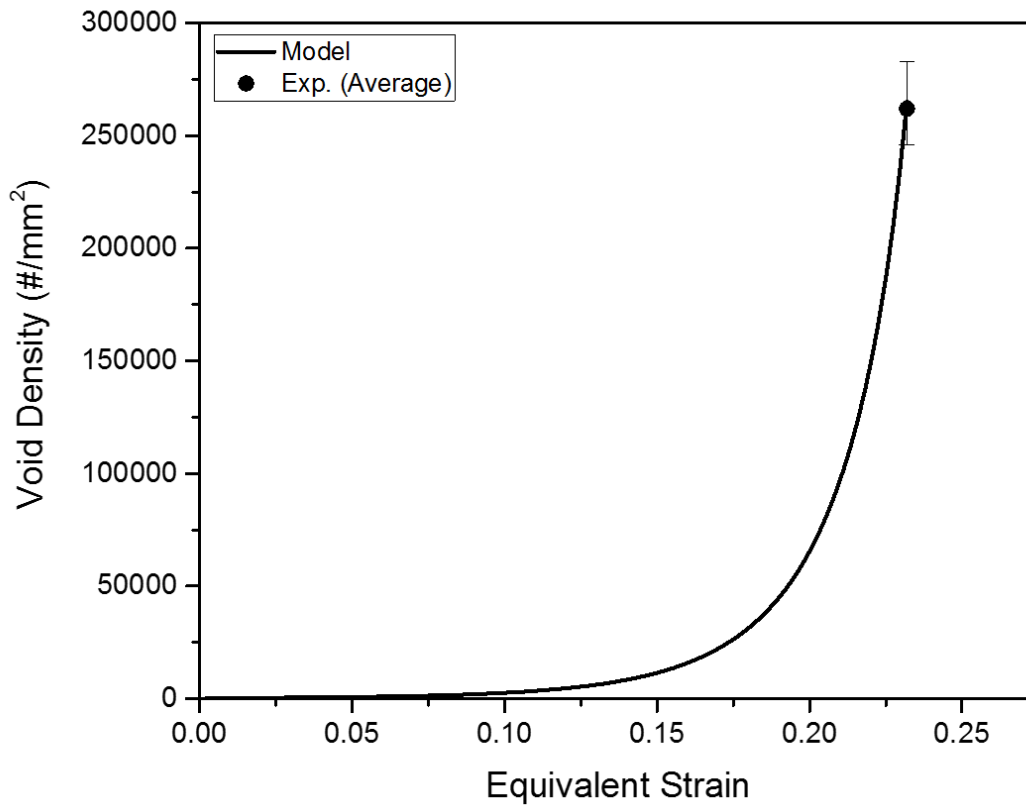


Figure 4-9. Comparison of the number density of voids on the fracture surface (average of experimental data) against the model prediction.

The experimentally determined void density was used as a calibration tool for the ISV plasticity-damage model accurately captures the damage nucleation in the experiments.

4.4. Conclusion

The material microstructure for the AA2219AFS-Deposition appears to be identical in the three orientations, with equiaxed grains of approximate 2.5 μm in size. SEM imaging showed θ particles that were also uniform in the three orientations. With the addition of microstructural characterization, the calibration of the ISV plasticity-damage model was performed using DMGFIT to capture one set of material constant for the whole dataset (see appendix A, Table 4-

A1 and 4-A2). Furthermore, BE experiments of tension followed by compression and compression followed by tension for the AFS-Deposition AA2219 depicted an asymmetric behavior where the kinematic hardening was greater than the isotropic hardening that the ISV plasticity-damage model was able to capture.

CHAPTER 5 CONCLUSIONS AND RECOMMENDATIONS

5.1. Conclusions

This dissertation is the first to detail the microstructural evolution and mechanical properties of solid-state, additively manufactured IN625 and AA2219 using a thermo-mechanical AFS-Deposition process. Aeroprobe Corporation provided the as-deposited material for both, IN625 and AA2219. Microstructural characterization for both materials was conducted to elucidate the beneficial 3D microstructure obtained from this new manufacturing process. To understand the material behavior under different loading rates and stress-states, tensile and compression experiments were performed at quasi-static (QS) and high strain rates (HR).

For the AFS-Deposited IN625, the EBSD results detailed a significantly refined, equiaxed grain structure, which was likely produced by continuous DRX during AFS-Deposition processing. The region with finer grain microstructure was localized to interface layers that separated macroscale layers formed by repeated passes of the AFS-Deposition tool. Furthermore, EBSD observed grains as fine as 0.27 microns in these layer interface regions, while the average grain size was approximately 1 micron in other regions of the deposited layers. The strain rate dependence of these fine-grained materials were examined at both QS (0.001/s) and HR (1500/s) strain rates using servo hydraulic and a direct tension-Kolsky bar, respectively, exhibiting both increases in yield and ultimate tensile strengths as strain rate increased. Additionally, when compared to other processing methods for IN625, the AFS-Deposition

results displayed comparable values to the reported FSW UTS data, but significantly higher YS and UTS than cast, wrought, or fusion-based AM data.

In the case of AFS-Deposited AA2219, EBSD results revealed a refined, equiaxed microstructure which is likely due to DRX [16–18]. A uniform grain size was found from the top to the bottom of the AFS-Deposition cross-section. The material hardness had a small variation from top to bottom, but taking into consideration the scatter in the data one could not statistically define any significant difference in hardness from the bottom to the top of the deposition. Further EBSD analysis of PFs showed that the material has a strong torsional fiber A texture in the top of the build, and this texture gets weaker in the middle and bottom sections. At lower length scales, TEM showed that there are no θ' precipitates in the as-deposited cross-section, therefore no precipitation strengthening should be expected.

The mechanical properties of the as-built AFS-Deposition AA2219 material are better than AA2219-O, but the YS and UTS values are below those of AA2219-T851 since there are no θ' precipitates providing strength to the material. The AFS AA2219 achieved higher ductility than AA2219-O and even AA2219-T851. As mentioned previously, research by Taminger and Hafley [29] showed that after applying the T62 temper to the as-built EBF material, the materials mechanical properties matched those of a AA2219-T62. This is extremely important, suggesting that the AFS-Deposited AA2219 should be able to regain the microstructural features and mechanical properties in the T62 and T851 tempers that are crucial for component level use. The strain rate dependence was examined, and at HR the material experienced higher yield strength and lower ultimate strength. At HR, the material strain hardening was less than when tested at QS, where one observes that the material stress-strain curve plateaus after yielding. In addition, the HR tensile specimens also exhibited more ϵ_f than the QS tensile specimens.

Lastly for the AFS-Deposited AA2219, the calibration of the ISV plasticity-damage model was performed using DMGFIT to capture one set of material constant for the whole dataset (see Appendix A, Table A1 and A2). The ISV plasticity-damage model successfully predicted the nucleation damage for the fractured tensile specimens. Furthermore, BE experiments of tension followed by compression and compression followed by tension for the AFS-Deposition AA2219 depicted an asymmetric behavior where the kinematic hardening was greater than the isotropic hardening that the ISV plasticity-damage model was able to capture.

Recommendations and Future Work

In summary, AFS-Deposition is a revolutionary new technology, with plenty of research still required to fully understand and optimize the materials synthesized through this thermo-mechanical solid-state additive manufacturing process.

- For the IN625, future research including texture evolution analysis, intermediate tensile experiments, compression experiments, fatigue, fracture toughness, nanoindentation, and transmission electron microscopy, will assist in elucidating the unique features resulting from this process and the respective influence on mechanical behavior.
- Many of the applications of AA2219 will benefit from intermediate tensile and compressive experiments, elevated and cryogenic tensile and compressive experiments, fracture toughness, corrosion, and fatigue experiments to understand material behavior.
- Additional research on optimizing the AFS process to avoid losing the θ' precipitates is suggested.
- Research on solutionizing and aging on the as-built AFS-Deposition AA2219 should be performed to restore the mechanical properties to AA2219-T62 and -T851.

- Interrupted notch Bridgman tensile specimen experiments are suggested to measure the damage at specific strain levels, and further validate the model.
- Processing studies to optimize the material microstructure and performance should be done.

REFERENCES

- [1] V. Shankar, M. Valsan, K.B.S. Rao, S.L. Mannan, Effects of temperature and strain rate on tensile properties and activation energy for dynamic strain aging in alloy 625, *Metall. Mater. Trans. A.* 35 (2004) 3129–3139. doi:10.1007/s11661-004-0057-0.
- [2] G.P. Dinda, A.K. Dasgupta, J. Mazumder, Laser aided direct metal deposition of Inconel 625 superalloy: Microstructural evolution and thermal stability, *Mater. Sci. Eng. A.* 509 (2009) 98–104. doi:10.1016/j.msea.2009.01.009.
- [3] K.H. Song, K. Nakata, Mechanical Properties of Friction-Stir-Welded Inconel 625 Alloy, *Mater. Trans.* 50 (2009) 2498–2501. doi:10.2320/matertrans.M2009200.
- [4] C.P. Paul, P. Ganesh, S.K. Mishra, P. Bhargava, J. Negi, A.K. Nath, Investigating laser rapid manufacturing for Inconel-625 components, *Opt. Laser Technol.* 39 (2007) 800–805. doi:10.1016/j.optlastec.2006.01.008.
- [5] Q. Guo, D. Li, S. Guo, H. Peng, J. Hu, The effect of deformation temperature on the microstructure evolution of Inconel 625 superalloy, *J. Nucl. Mater.* 414 (2011) 440–450. doi:10.1016/j.jnucmat.2011.05.029.
- [6] F. Xu, Y. Lv, Y. Liu, F. Shu, P. He, B. Xu, Microstructural Evolution and Mechanical Properties of Inconel 625 Alloy during Pulsed Plasma Arc Deposition Process, *J. Mater. Sci. Technol.* 29 (2013) 480–488. doi:10.1016/j.jmst.2013.02.010.
- [7] S. Li, Q. Wei, Y. Shi, Z. Zhu, D. Zhang, Microstructure Characteristics of Inconel 625 Superalloy Manufactured by Selective Laser Melting, *J. Mater. Sci. Technol.* 31 (2015) 946–952. doi:10.1016/j.jmst.2014.09.020.
- [8] W. Xu, J. Liu, G. Luan, C. Dong, Temperature evolution, microstructure and mechanical properties of friction stir welded thick 2219-O aluminum alloy joints, *Mater. Des.* 30 (2009) 1886–1893. doi:10.1016/j.matdes.2008.09.021.
- [9] Q. Li, A. Wu, Y. Li, G. Wang, D. Yan, J. Liu, Influence of temperature cycles on the microstructures and mechanical properties of the partially melted zone in the fusion welded joints of 2219 aluminum alloy, *Mater. Sci. Eng. A.* 623 (2015) 38–48. doi:10.1016/j.msea.2014.11.047.
- [10] W.M.W. Thomas, I. Norris, E.D. Nicholas, J.C. Needham, M.G. Murch, P. Temple-Smith, et al., *Friction stir welding—process developments and variant techniques*, 1991.

- http://www.google.com/patents/US5460317%5Cnhttp://scholar.google.com/scholar?hl=en&btnG=Search&q=intitle:5,460,317#3%5Cnhttp://scholar.google.com/scholar?hl=en&btnG=Search&q=intitle:5460317#3%5Cnhttp://hegesztesportal.hu/hegesztes/tudastar/wt_fsw.pdf.
- [11] B. Li, Y. Shen, W. Hu, The study on defects in aluminum 2219-T6 thick butt friction stir welds with the application of multiple non-destructive testing methods, *Mater. Des.* 32 (2011) 2073–2084. doi:10.1016/j.matdes.2010.11.054.
- [12] G. Cao, S. Kou, Friction Stir Welding of 2219 Aluminum: Behavior of θ (Al₂Cu) particles, *Weld. J.* 84 (2005) 1–8.
- [13] M. Eskandari, A. Najafizadeh, A. Kermanpur, M. Karimi, Potential application of nanocrystalline 301 austenitic stainless steel in lightweight vehicle structures, *Mater. Des.* 30 (2009) 3869–3872. doi:10.1016/j.matdes.2009.03.043.
- [14] J.Q. Su, T.W. Nelson, R. Mishra, M. Mahoney, Microstructural investigation of friction stir welded 7050-T651 aluminium, *Acta Mater.* 51 (2003) 713–729. doi:10.1016/S1359-6454(02)00449-4.
- [15] J.Q. Su, T.W. Nelson, C.J. Sterling, Friction stir processing of large-area bulk UFG aluminum alloys, *Scr. Mater.* 52 (2005) 135–140. doi:10.1016/j.scriptamat.2004.09.014.
- [16] J. Su, T.W. Nelson, C.J. Sterling, A new route to bulk nanocrystalline materials, *J. Mater. Res.* 18 (2003) 1757–1760.
- [17] J. Su, T.W. Nelson, C.J. Sterling, Grain refinement of aluminum alloys by friction stir processing, *Philos. Mag.* 86 (2006) 1–24. doi:10.1023/A:1012882413401.
- [18] J.-Q. Su, T.W. Nelson, C.J. Sterling, Microstructure evolution during FSW/FSP of high strength aluminum alloys, *Mater. Sci. Eng. A.* 405 (2005) 277–286. doi:10.1016/j.msea.2005.06.009.
- [19] N. Saito, I. Shigematsu, T. Komaya, T. Tamaki, G. Yamauchi, M. Nakamura, Grain refinement of 1050 aluminum alloy by friction stir processing, *J. Mater. Sci. Lett.* 86 (2001) 1913–1915. doi:10.1023/A:1012882413401.
- [20] R.D. Doherty, D.A. Hughes, F.J. Humphreys, J.J. Jonas, D.J. Jensen, M.E. Kassner, et al., Current issues in recrystallization: a review, *Mater. Sci. Eng. A.* 238 (1997) 219–274. doi:10.1016/S0921-5093(97)00424-3.
- [21] J.Q. Su, T.W. Nelson, T.R. McNelley, R.S. Mishra, Development of nanocrystalline structure in Cu during friction stir processing (FSP), *Mater. Sci. Eng. A.* 528 (2011) 5458–5464. doi:10.1016/j.msea.2011.03.043.
- [22] G.V. Narayana, V.M.J. Sharma, V. Diwakar, K.S. Kumar, R.C. Prasad, Fracture

- behaviour of aluminium alloy 2219–T87 welded plates, *Sci. Technol. Weld. Join.* 9 (2004) 121–130. doi:10.1179/136217104225017035.
- [23] K. Elangovan, V. Balasubramanian, S. Babu, Developing an empirical relationship to predict tensile strength of friction stir welded AA2219 aluminum alloy, *J. Mater. Eng. Perform.* 17 (2008) 820–830. doi:10.1007/s11665-008-9240-6.
- [24] J.A. Hartman, R.J. Beil, G.T. Hahn, Effect of Copper-Rich Regions on Tensile Properties of VPPA Weldments of 2219-T87 Aluminum, (n.d.).
- [25] H. Doude, J. Schneider, B. Patton, S. Stafford, T. Waters, C. Varner, Optimizing weld quality of a friction stir welded aluminum alloy, *J. Mater. Process. Technol.* 222 (2015) 188–196. doi:10.1016/j.jmatprotec.2015.01.019.
- [26] R.I. Rodriguez, J.B. Jordon, H.M. Rao, H. Badarinarayan, W. Yuan, H. El Kadiri, et al., Microstructure, texture, and mechanical Properties of friction stir spot welded rare-earth containing magnesium ZEK100 alloy sheets, *Mater. Sci. Eng. A.* (2014). doi:10.1016/j.msea.2014.09.010.
- [27] R.I. Rodriguez, J.B. Jordon, P.G. Allison, T. Rushing, L. Garcia, Microstructure and mechanical properties of dissimilar friction stir welding of 6061-to-7050 aluminum alloys, *Mater. Des.* 83 (2015) 60–65. doi:10.1016/j.matdes.2015.05.074.
- [28] B. Li, Y. Shen, The investigation of abnormal particle-coarsening phenomena in friction stir repair weld of 2219-T6 aluminum alloy, *Mater. Des.* 32 (2011) 3796–3802. doi:10.1016/j.matdes.2011.03.029.
- [29] K.M. Taminger, R.A. Hafley, Electron beam freeform fabrication: a rapid metal deposition process, *Proc. 3rd Annu. Automot. Compos. Conf.* (2003) 9–10. http://www.ntrs.nasa.gov/archive/nasa/casi.ntrs.nasa.gov/20040042496_2004036110.pdf.
- [30] K.M. Taminger, R.A. Hafley, Electron beam freeform fabrication for cost effective near-net shape manufacturing, *Nato Avt.* 139 (2006).
- [31] K.M.B. Taminger, R.A. Hafley, Characterization of 2219 Aluminum Produced by Electron Beam Freeform Fabrication, in: *13th Solid Free. Fabr. Symp.*, 2002.
- [32] V. Shankar, K. Bhanu Sankara Rao, S.L. Mannan, Microstructure and mechanical properties of Inconel 625 superalloy, *J. Nucl. Mater.* 288 (2001) 222–232. doi:10.1016/S0022-3115(00)00723-6.
- [33] E.E. Brown, D.R. Muzyka, *The Superalloys II*, Wiley, New York, NY, 1987.
- [34] C.T. Sims, A History of Superalloy Metallurgy for Superalloy Metallurgists, *Statew. Agric. L. Use Baseline* 2015. 1 (2015) 399–419. doi:10.1017/CBO9781107415324.004.

- [35] A. Enes, A. Gürsel, A Review on Superalloys and IN718 Nickel-Based INCONEL Superalloy, *Period. Engineering Nat. Sci.* 1 (2013).
- [36] R.C. Reed, *The Superalloys: Fundamentals and Applications*, Cambridge Univ. Press. UK. (2006).
- [37] J. Schultz, K. Creehan, *System for continuous feeding of filler material for friction stir welding, processing and fabrication*, 2014.
- [38] L. Xue, M.U. Islam, Free-form laser consolidation for producing metallurgically sound and functional components, *J. Laser Appl.* 12 (2000) 160. doi:10.2351/1.521927.
- [39] P. Ganesh, R. Kaul, C.P. Paul, P. Tiwari, S.K. Rai, R.C. Prasad, et al., Fatigue and fracture toughness characteristics of laser rapid manufactured Inconel 625 structures, *Mater. Sci. Eng. A.* 527 (2010) 7490–7497. doi:10.1016/j.msea.2010.08.034.
- [40] M. Rombouts, G. Maes, M. Mertens, W. Hendrix, Laser metal deposition of Inconel 625: Microstructure and mechanical properties, *J. Laser Appl.* 24 (2012) 52007. doi:10.2351/1.4757717.
- [41] L.E. Murr, E. Martinez, S.M. Gaytan, D.A. Ramirez, B.I. MacHado, P.W. Shindo, et al., Microstructural architecture, microstructures, and mechanical properties for a nickel-base superalloy fabricated by electron beam melting, *Metall. Mater. Trans. A Phys. Metall. Mater. Sci.* 42 (2011) 3491–3508. doi:10.1007/s11661-011-0748-2.
- [42] K. Amato, Comparison of Microstructures and Properties for a Ni-Base Superalloy (Alloy 625) Fabricated by Electron Beam Melting, *J. Mater. Sci. Res.* 1 (2012) p3. doi:10.5539/jmsr.v1n2p3.
- [43] G.L. Erickson, Polycrystalline Cast Superalloys, in: *Met. Handb. Vol. 1, 10th ed.*, ASM International, Materials Park, OH, 1990: pp. 981–994.
- [44] N.S. Stoloff, Wrought and P/M Superalloys, in: *Met. Handb. Vol. 1, 10th ed.*, ASM International, Materials Park, OH, 1990: pp. 950–977.
- [45] R.S. Mishra, Z.Y. Ma, Friction stir welding and processing, *Mater. Sci. Eng. R Reports.* 50 (2005) 1–78. doi:10.1016/j.mser.2005.07.001.
- [46] R.I. Rodriguez, J.B. Jordon, P.G. Allison, T. Rushing, L. Garcia, Microstructure and mechanical properties of dissimilar friction stir welding of 6061-to-7050 aluminum alloys, *Mater. Des.* 83 (2015) 60–65. doi:10.1016/j.matdes.2015.05.074.
- [47] R.I.I. Rodriguez, J.B.B. Jordon, P.G.G. Allison, T. Rushing, L. Garcia, Low-cycle fatigue of dissimilar friction stir welded aluminum alloys, *Mater. Sci. Eng. A.* 654 (2016) 236–248. doi:10.1016/j.msea.2015.11.075.

- [48] F. Ye, H. Fujii, T. Tsumura, K. Nakata, Friction stir welding of Inconel alloy 600, *J. Mater. Sci.* 41 (2006) 5376–5379. doi:10.1007/s10853-006-0169-6.
- [49] Military Handbook Metallic Materials and Elements for Aerospace Vehicle Structures, 1998.
- [50] W.R. Whittington, a. L. Oppedal, S. Turnage, Y. Hammi, H. Rhee, P.G. Allison, et al., Capturing the effect of temperature, strain rate, and stress state on the plasticity and fracture of rolled homogeneous armor (RHA) steel, *Mater. Sci. Eng. A.* 594 (2014) 82–88. doi:10.1016/j.msea.2013.11.018.
- [51] O.L. Rodriguez, P.G. Allison, W.R. Whittington, D.K. Francis, O.G. Rivera, K. Chou, et al., Dynamic tensile behavior of electron beam additive manufactured Ti6Al4V, *Mater. Sci. Eng. A.* 641 (2015) 323–327. doi:10.1016/j.msea.2015.06.069.
- [52] J.P. Lewis, Fast Template Matching Template Matching by Cross Correlation 2 Normalized Cross Correlation Normalized Cross Correlation in the Transform Domain, *Pattern Recognit.* 10 (1995) 120–123. <http://citeseerx.ist.psu.edu/viewdoc/download?doi=10.1.1.157.3888&rep=rep1&type=pdf>.
- [53] R.M. Haralick, L.G. Shapiro, *Computer Robot Vision*, Vol 2, Addison-Wesley, 1992.
- [54] D. Francis, W.R. Whittington, W.B. LawrimoreII, P.G. Allison, S.A. Turnage, J.J. Bhattacharyya, Split Hopkinson Pressure Bar Graphical Analysis Tool, 57 (2017) 179–183.
- [55] L.N. Brewer, D.P. Field, C.C. Merriman, Mapping and Assessing Plastic Deformation Using EBSD, in: *Electron Backscatter Diffr. Mater. Sci.*, Springer US, Boston, MA, 2009: pp. 251–262. doi:10.1007/978-0-387-88136-2_18.
- [56] F.J. Humphreys, A unified theory of recovery, recrystallization and grain growth, based on the stability and growth of cellular microstructures—I. The basic model, *Acta Mater.* 45 (1997) 4231–4240. doi:10.1016/S1359-6454(97)00070-0.
- [57] B.W. Baker, E.S.K. Menon, T.R. Mcnelley, L.N. Brewer, B. El-Dasher, J.C. Farmer, et al., Processing-Microstructure Relationships in Friction Stir Welding of MA956 Oxide Dispersion Strengthened Steel, *Metall. Mater. Trans. E.* 1 (2014) 318–330. doi:10.1007/s40553-014-0033-6.
- [58] Z. Wang, K. Guan, M. Gao, X. Li, X. Chen, X. Zeng, The microstructure and mechanical properties of deposited-IN718 by selective laser melting, *J. Alloys Compd.* 513 (2012) 518–523. doi:10.1016/j.jallcom.2011.10.107.
- [59] J. Kang, Z.C. Feng, J.C. Li, G.S. Frankel, G.Q. Wang, A.P. Wu, Friction Stir Welding of Al Alloy 2219-T8: Part I- Evolution of Precipitates and Formation of Abnormal Al₂Cu, *Metall. Mater. Trans. A Phys. Metall. Mater. Sci.* 47A (2016) 4553–4565.

- doi:10.1007/s11661-016-3648-7.
- [60] J. Kang, Z.C. Feng, J.C. Li, G.S. Frankel, G.Q. Wang, A.P. Wu, Friction Stir Welding of Al Alloy 2219-T8: Part II-Mechanical and Corrosion, *Metall. Mater. Trans. A Phys. Metall. Mater. Sci.* 47A (2016) 4566–4577. doi:10.1007/s11661-016-3646-9.
- [61] J.G. Kaufman, *Introduction to Aluminum Alloys and Tempers*, ASM International, Metals Park, OH, 2000.
- [62] P.G. Allison, H. Grewal, Y. Hammi, H.R. Brown, W.R. Whittington, M.F. Horstemeyer, Plasticity and Fracture Modeling/Experimental Study of a Porous Metal Under Various Strain Rates, Temperatures, and Stress States, *J. Eng. Mater. Technol.* 135 (2013) 41008. doi:10.1115/1.4025292.
- [63] P.G. Allison, M.F. Horstemeyer, Y. Hammi, H.R. Brown, M.T. Tucker, Y.K. Hwang, Microstructure-property relations of a steel powder metal under varying temperatures, strain rates, and stress states, *Mater. Sci. Eng. A.* 529 (2011) 335–344. doi:10.1016/j.msea.2011.09.037.
- [64] ASTM E384: Standard Test Method for Microindentation Hardness of Materials, *ASTM Int.* (2015) 1–24. doi:10.1520/E0384-16.
- [65] H. Al-Khalid, A. Alaskari, S. Oraby, Statistical and graphical assessment of circumferential and radial hardness variation of AISI 4140, AISI 1020 and AA 6082 aluminum alloy, *Materials (Basel)*. 5 (2012) 12–26. doi:10.3390/ma5010012.
- [66] H.W. Coleman, W.G. Steele, *Experimentation and Uncertainty Analysis for Engineers*, Second Edi, John Wiley & Sons, Inc, New York, NY, 1999.
- [67] F. Montheillet, M. Cohen, J.J. Jonas, Axial stresses and texture development during the torsion testing of Al, Cu and α -Fe, *Acta Metall.* 32 (1984) 2077–2089. doi:10.1016/0001-6160(84)90187-1.
- [68] R.W. Fonda, J.F. Bingert, Texture variations in an aluminum friction stir weld, *Scr. Mater.* 57 (2007) 1052–1055. doi:10.1016/j.scriptamat.2007.06.068.
- [69] M.F. Horstemeyer, A.M. Gokhale, A Void-Crack Nucleation Model for Ductile Metals, *Int. J. Solids Struct.* 36 (1999) 5029–5055. doi:10.1016/S0020-7683(98)00239-X.
- [70] S. Brauer, W.R. Whittington, K. Johnson, B. Li, H. Rhee, P. Allison, et al., Strain rate and stress state dependence of gray cast iron, *J. Eng. Mater. Technol.* (n.d.).
- [71] M.F. Horstemeyer, S. Ramaswamy, M. Negrete, Using a micromechanical finite element parametric study to motivate a phenomenological macroscale model for void/crack nucleation in aluminum with a hard second phase, *Mech. Mater.* 35 (2003) 675–687. doi:10.1016/S0167-6636(02)00165-5.

- [72] M. Horstemeyer, D. McDowell, J. Fan, From atom to autos, a new design paradigm using microstructure-property modelling, *Monotonic Load. Cond. Sandia ... Part 1: Mo* (2001). <http://scholar.google.com/scholar?hl=en&btnG=Search&q=intitle:from+atoms+to+autos:+A+New+Design+Paradigm+Using+microstructure-property+modeling#3>.
- [73] K.N. Solanki, M.F. Horstemeyer, W.G. Steele, Y. Hammi, J.B. Jordon, Calibration, validation, and verification including uncertainty of a physically motivated internal state variable plasticity and damage model, *Int. J. Solids Struct.* 47 (2010) 186–203. doi:10.1016/j.ijsolstr.2009.09.025.
- [74] M.F. Horstemeyer, D.J. Bammann, Historical review of internal state variable theory for inelasticity, *Int. J. Plast.* 26 (2010) 1310–1334. doi:10.1016/j.ijplas.2010.06.005.
- [75] J.B. Jordon, M.F. Horstemeyer, K. Solanki, J.D. Bernard, J.T. Berry, T.N. Williams, Damage characterization and modeling of a 7075-T651 aluminum plate, *Mater. Sci. Eng. A.* 527 (2009) 169–178. doi:10.1016/j.msea.2009.07.049.
- [76] M.F. Horstemeyer, *Integrated Computational Materials Engineering (ICME) for Metals*, John Wiley & Sons, Inc, Hoboken, New Jersey, 2012.
- [77] D.J. Bammann, E.C. Aifantis, A damage model for ductile metals, *Nucl. Eng. Des.* 116 (1989) 355–362. doi:10.1016/0029-5493(89)90095-2.
- [78] D.J. Bammann, M.L. Chiesa, G.C. Johnson, Modeling large deformation and failure in manufacturing processes, *Teor. Appl. Mech.* (1996) 256–276.
- [79] J. Bauschinger, Changes of the elastic limit and the modulus of elasticity on various metals, *Civilingenieur.* 27 (1881) 289–348.
- [80] T. Kishi, T. Tanabe, The Bauschinger effect and its role in mechanical anisotropy, *J. Mech. Phys. Solids.* 21 (1973) 303–315. doi:10.1016/0022-5096(73)90002-1.
- [81] H. Margolin, F. Hazaveh, H. Yaguchi, The grain boundary contribution to the bauschinger effect, *Scr. Metall.* 12 (1978) 1141–1145.
- [82] T. Richeton, S. Berbenni, M. Berveiller, Grain-size dependent accommodation due to intragranular distributions of dislocation loops, *Acta Mater.* 57 (2009) 1347–1356. doi:10.1016/j.actamat.2008.11.024.
- [83] S.N. Buckley, K.M. Entwistle, The bauschinger effect in super-pure aluminum single crystals and polycrystals, *Acta Metall.* 4 (1956) 352–361. doi:10.1016/0001-6160(56)90023-2.
- [84] M.F. Horstemeyer, S. Ramaswamy, On Factors Affecting Localization and Void Growth in Ductile Metals: A Parametric Study, *Int. J. Damage Mech.* 9 (2000) 5–28. doi:10.1177/105678950000900102.

- [85] J.B. Jordon, M.F. Horstemeyer, K. Solanki, Y. Xue, Damage and stress state influence on the Bauschinger effect in aluminum alloys, *Mech. Mater.* 39 (2007) 920–931.
- [86] M. Miller, Reverse yield experiments and internal variable evolution in polycrystalline metals, *Int. J. Plast.* 15 (1999) 93–117. doi:10.1016/S0749-6419(98)00046-1.
- [87] T. Tang, Y. Hammi, M.F. Horstemeyer, P. Wang, Finite element micromechanical analysis of the deformation and stress state dependent damage evolution in fiber reinforced metal matrix composites, *Comput. Mater. Sci.* 59 (2012) 165–173.
- [88] R.R. Mccullough, *Microstructure-Sensitive Plasticity and Fatigue Modeling of Extruded 6061 Aluminum Alloys*, The University of Alabama, 2014.
- [89] C. Caceres, J. Griffiths, P. Reiner, The influence of microstructure on the Bauschinger effect in an Al-Si-Mg casting alloy, *Acta Mater.* 7151 (1996) 15–23.
- [90] M.F. Horstemeyer, Damage influence on Bauschinger effect of a cast A356 aluminum alloy, *Scr. Mater.* 39 (1998) 1491–1495. doi:10.1016/S1359-6462(98)00343-1.
- [91] J.D. Embury, Structural aspects of the Bauschinger effect, *Mater. Forum.* 10 (1987) 27–32.
- [92] M.F. Horstemeyer, J. Lathrop, a. M. Gokhale, M. Dighe, Modeling stress state dependent damage evolution in a cast Al–Si–Mg aluminum alloy, *Theor. Appl. Fract. Mech.* 33 (2000) 31–47. doi:10.1016/S0167-8442(99)00049-X.

APPENDIX

Nomenclature

- a = constant for nucleation equation
- b = constant for nucleation equation
- c = coalescence
- c_2 = constant for nucleation equation
- C_{TC} = temperature constant for coalescence equation
- $C_{T\eta}$ = constant for nucleation equation
- d = average inclusion particle size
- D_g = average inclusion particle size
- d_0 = pore diameter
- \underline{D} = rate of deformation
- \underline{D}^e = elastic rate of deformation
- \underline{D}^{in} = inelastic rate of deformation
- \underline{D}_d^p = isochoric inelastic rate of deformation
- \underline{D}_v^p = volumetric inelastic rate of deformation
- f = initial particle volume fraction
- F = deformation gradient
- $f(T)$ = rate sensitivity of yield
- \underline{F}^e = elastic portion of deformation gradient
- \underline{F}^p = inelastic portion of deformation gradient
- \underline{F}_d^p = isochoric inelastic portion of deformation gradient
- \underline{F}_v^p = volumetric inelastic portion of deformation gradient
- G = Shear modulus
- h = kinematic hardening modulus
- H = isotropic hardening modulus
- I = first stress invariant
- J = Jacobian
- J_2 = second deviatoric stress invariant
- J_3 = third deviatoric stress invariant
- K_{IC} = fracture toughness
- m = strain rate sensitivity parameter
- n = strain hardening exponent

- NND = pore nearest neighbor distance
 R = isotropic hardening modulus
 r_d = kinematic dynamic recovery
 r_s = kinematic static recovery
 R_0 = initial pore radius
 t = time
 T = temperature
 V = volume
 $V(T)$ = strain rate dependence on yield
 $Y(T)$ = rate independent yield
 α = kinematic hardening
 ξ = constant for coalescence equation
 ε = strain
 η = pore nucleation
 λ, μ = elastic Lamé constants
 ν = pore growth
 ρ = density
 σ = stress
 σ_e = equivalent Von Mises stress
 σ_h = hydrostatic stress
 φ = damage or volume fraction of pores

The pertinent equations in this model are denoted by the rate of change of the observable and internal state variables. The equations used within the context of the finite element method are given by,

$$\dot{\underline{\sigma}} = \dot{\underline{\sigma}} - \underline{W}^e \underline{\sigma} - \underline{\sigma} \underline{W}^e = \lambda(1-D)tr(\underline{D}^e)\underline{I} + 2\mu(1-D)(\underline{D}^e) - \frac{\dot{D}}{1-D}\underline{\sigma}$$

Equation A.1

$$\underline{D}^e = \underline{D} - \underline{D}^{in}$$

Equation A.2

$$\underline{D}^{in} = f(T) \sinh \left[\frac{\|\underline{\sigma}' - \underline{\alpha}\| - \{R + Y(T)\}\{1-D\}}{V(T)\{1-D\}} \right] \frac{\underline{\sigma}' - \underline{\alpha}}{\|\underline{\sigma}' - \underline{\alpha}\|}$$

Equation A.3

$$\dot{\underline{\alpha}} = \dot{\underline{\alpha}} - \underline{W}^e \underline{\alpha} + \underline{\alpha} \underline{W}^e = \left\{ h\{T\} \underline{D}^{in} - \left[\sqrt{\frac{2}{3}} r_d(T) \|\underline{D}^{in}\| + r_s(T) \right] \|\underline{\alpha}\| \underline{\alpha} \right\} \left[\frac{DCS_0}{DCS} \right]^z$$

Equation A.4

$$\dot{R} = \left\{ H \{T\} \underline{D}^{in} - \left[\sqrt{\frac{2}{3}} R_d(T) \|\underline{D}^{in}\| + R_s(T) \right] R^2 \right\} \left[\frac{DCS_0}{DCS} \right]^z$$

Equation A.5

$$\dot{D} = \left[\dot{\phi}_{particles} + \dot{\phi}_{pores} \right] c + \left[\dot{\phi}_{particles} + \dot{\phi}_{pores} \right] \dot{c}$$

Equation A.6

$$\dot{\phi}_{particles} = \dot{\eta} \nu + \eta \dot{\nu}$$

Equation A.7

$$\dot{\eta} = \|\underline{D}^{in}\| \frac{d^{1/2}}{K_{IC} f^{1/3}} \eta \left\{ a \left[\frac{4}{27} - \frac{J_3^2}{J_2^3} \right] + b \frac{J_3}{J_2^{3/2}} + c \left\| \frac{I_1}{\sqrt{J_2}} \right\| \right\} \exp\left(-C_{\eta T}/T\right)$$

Equation A.8

$$\dot{\nu} = \frac{3}{2} \nu \left[\frac{3 V(T) \sigma_H}{2 Y(T) \sigma_{vm}} + \left(1 - \frac{V(T)}{Y(T)}\right) (1 + 0.4319) \right]^{Y(T)/\nu(T)} \underline{D}^{in}$$

Equation A.9

$$\dot{c} = C_{coal} \left[\eta \dot{\nu} + \dot{\eta} \nu \right] \exp(C_{CT} T) \left(\frac{DCS_0}{DCS} \right)^z$$

Equation A.10

$$\dot{\phi}_{pores} = \left[\frac{1}{(1 - \phi_{pores})^m} - (1 - \phi_{pores}) \right] \sinh \left\{ \frac{2 \left((2^{\nu(T)}/Y(T)) - 1 \right) \sigma_H}{\left((2^{\nu(T)}/Y(T)) + 1 \right) \sigma_{vm}} \right\} \|\underline{D}^{in}\|$$

Equation A.11

The internal state variable equations A.4-A.11, shown in Appendix A, are function of visible variables such as temperature, stress state, and rate of deformation. Rate equations are usually written to exhibit objectivity rates $(\overset{\circ}{\sigma}, \overset{\circ}{\alpha})$, that are indifferent of the reference frame. In this sense, rate equations differs from a Jaumann rate, which assumes the continuum spins equals elastic spin ($\underline{W} = \underline{W}^e$). This model also incorporates deviatoric inelastic deformation, result of existence of dislocations in crystallographic materials, dilational deformation, and resultant failure caused by damage progression.

Constants such as the elastic Lamé constants (λ and μ) are incorporated in equation A.1, and the total deformation (\underline{D}) defined by the boundary conditions is subtracted from the flow rule in equation A.2, which results in the elastic rate deformation (\underline{D}^e). The quantity of damage, D , is a scalar that should not be confused with the second rank tensors mentioned above.

Creep and plasticity regimes in equation A.3 are comprised by the deviatoric inelastic flow rule, $\underline{D}^{\text{in}}$, a function of temperature, stress, kinematic hardening ISV ($\underline{\alpha}$), isotropic hardening ISV (\underline{R}), volume fraction of damaged material (D), and functions $f(T)$, $V(T)$, and $Y(T)$, which have an Arrhenius-type temperature dependence related to yielding. Rate independence yield stress is found from $Y(T)$, and the initial yielding that is affected by the rate dependence is determined from $f(T)$. The magnitude of rate dependence on yielding is determined by $V(T)$. Monotonic compression, tension, and torsion tests at different temperatures and strain rates are used to determine functions $f(T)$, $V(T)$, and $Y(T)$.

The hardening equations A.4 and A.5, include dynamic and static recovery with the kinematic and isotropic hardening modulus, $h(T)$ and $H(T)$, respectively. Static and dynamic recovery are defined by the scalar functions $r_s(T)$ and $R_s(T)$, and $r_d(T)$ and $R_d(T)$, respectively.

Table A1. Elastic and plastic constants for AFS AA2219.

AFS AA2219	Constants	Value	Units
Elastic and thermal constants	Shear Modulus,	27,862.60	MPa
	G		
	a	0	
	Bulk Modulus,	73,000	MPa
K			
	b	0	

	Init. Temperature	297	K
	Melt Temperature	821	K
	Heat gen. coeff.	0.34	
Yield and yield adjustment constants	C1	0	MPa
	C2	0	K
	C3	115	MPa
	C4	60	K
	C5	1	1/MPa
	C6	0	K
	C19	0	
	C20	0	1/K
Kinematic hardening and recovery constants	C7	0.05	1/MPa
	C8	0.05	K
	C9	1700	MPa
	C10	0.1	K
	C11	0	s/MPa
	C12	0	K
Isotropic Hardening and recovery constants	C13	0.019	1/MPa
	C14	0	K
	C15	2200	MPa
	C16	1.7	K
	C17	0	s/MPa
	C18	0	K
Cyclic Hardening and recovery	C21	7	1/MPa
	C22	668.26	K
	C23	0	MPa
	C24	0	MPa/K
	C25	0	1/MPa*s
Hardening and recovery	Ca	0	
	Cb	-0.4	

Table A2. Damage model constants for AFS AA2219.

AFS AA2219	Constants	Value	Units
McClintock void growth constants	Void growth exp.	0.3	
	Init. rad.	0.002	mm
Nucleation	a	475	

	b	9000	
	c	750	
	Nuc. Coeff.	255	
	Fract. Toughness	33	MPa/m ^{1/2}
	Part. Size	0.0014	mm
	Part. vol. fract.	0.037	
Coalescence	cd1	0.1	
	cd2	0	
	dsc0	.0025	mm
	dcs	.0025	mm
	dcs exp. Zz	0	
CApore growth	Init. void vol. fract	0.0001	
Nucleation	Nuc. temp., depend.	-65	
Coalescence	Coal. temp., depend	0	
